Spatial Position Regulates Power of Tryptophan: Discovery of a Major-Groove-Specific Nuclear-Localizing, Cell-Penetrating Tetrapeptide

Debmalya Bhunia,[†,#] Prasenjit Mondal,[†,‡,#] Gaurav Das,[†,‡] Abhijit Saha,[†,⊥] Pallabi Sengupta,[§,⊥] Jagannath Jana,[§] Saswat Mohapatra,[†,‡] Subhrangsu Chatterjee,[§] and Surajit Ghosh[*,†,‡]

[†]Organic and Medicinal Chemistry Division, CSIR-Indian Institute of Chemical Biology, 4, Raja S. C. Mullick Road, Kolkata 700032, India

[‡]Academy of Scientific & Innovative Research (AcSIR), CSIR-Indian Institute of Chemical Biology, 4, Raja S. C. Mullick Road, Kolkata 700032, India

[§]Department of Biophysics, Bose Institute, P-1/12 CIT Scheme VII (M), Kolkata 700054, India

S Supporting Information

ABSTRACT: Identification of key amino acids is required for development of efficient cell-penetrating peptides (CPPs) and has tremendous implications in medicine. Extensive research work has enlightened us about the importance of two amino acids, arginine and tryptophan, in cell penetration. Here, we present a top-down approach to show how spatial positions of two tryptophans regulate the cellular entry and nuclear localization. This enables us to develop short, non-toxic tetrapeptides with excellent potential for cell penetration and nuclear localization. Among them, Glu-Thr-Trp-Trp (ETWW) emerges as the most promising. Results suggest that it enters into cancer cells following an endocytic pathway and binds at the major groove of nuclear DNA, where successive tryptophan plays major role. We subsequently show that it is not a P-glycoprotein substrate and is non-toxic to PC12-derived neurons, suggesting its excellent potential as a CPP. Furthermore, its potential as a CPP is validated in multi-cellular 3D cell culture (spheroid) and in *in vivo* mice model. This study provides major fundamental insights about the positional importance of tryptophan and opens new avenues toward the development of next-generation CPPs and major-groove-specific anticancer drugs.
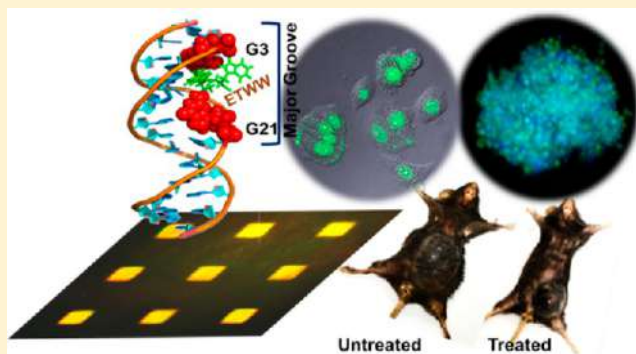
1. INTRODUCTION

Plasma membrane remains a tough barrier for smooth entry of drugs, causing poor cellular uptake and requiring high amounts of drugs to be administered to achieve the desired biological effect. Thus, efficient translocation of a drug through the plasma membrane is extremely important for its successful delivery and minimization of side effects on healthy tissues. This issue has been addressed in remarkable studies such as the identification of the Trans-activator of Transcription (Tat) protein of the human immunodeficiency virus (HIV)[1,2] and *Drosophila melanogaster* Antennapedia homeodomain[3] as important structural sequences for efficient translocation into cells. Further studies have revealed the minimum domain needed for translocation, popularly termed as "cell-penetrating peptides" (CPPs).[4−6] Numerous reports have highlighted the importance of arginine as a basic amino acid in CPPs, due to the bidentate H-bonding interaction through the guanidinium group of arginine and phosphate groups in the membrane.[7−12] Similarly, several reports have highlighted the influence of tryptophan residues compared to arginine in cell penetra-

tion.[4,13] Further studies have revealed that tryptophan and other aromatic amino acid residues involved in membrane destabilization interact with the plasma membrane bilayer and facilitate translocation through hydrophobic interactions.[14−21] In this context, a CPP has been designed, popularly known as Pep1 and marketed as "Chariot", which contains a tryptophan-rich hydrophobic motif (16-mer peptide) for translocation across the membrane and is additionally tagged with a basic hexapeptide as a nuclear localizing sequence through a tripeptide spacer[22,23] (Figure 1a). Although it can efficiently enter into cultured cells, can localize into the nucleus, and is capable of delivering various therapeutic peptides and proteins into the cultured cells in functional form, the mechanism of entry and the rationale for using a long hydrophobic sequence is poorly understood.[24−28] An important point to be noted is that long CPPs such as Tat cause amyloidogenecity in the brain.[29] Therefore, the question remains, do we need long
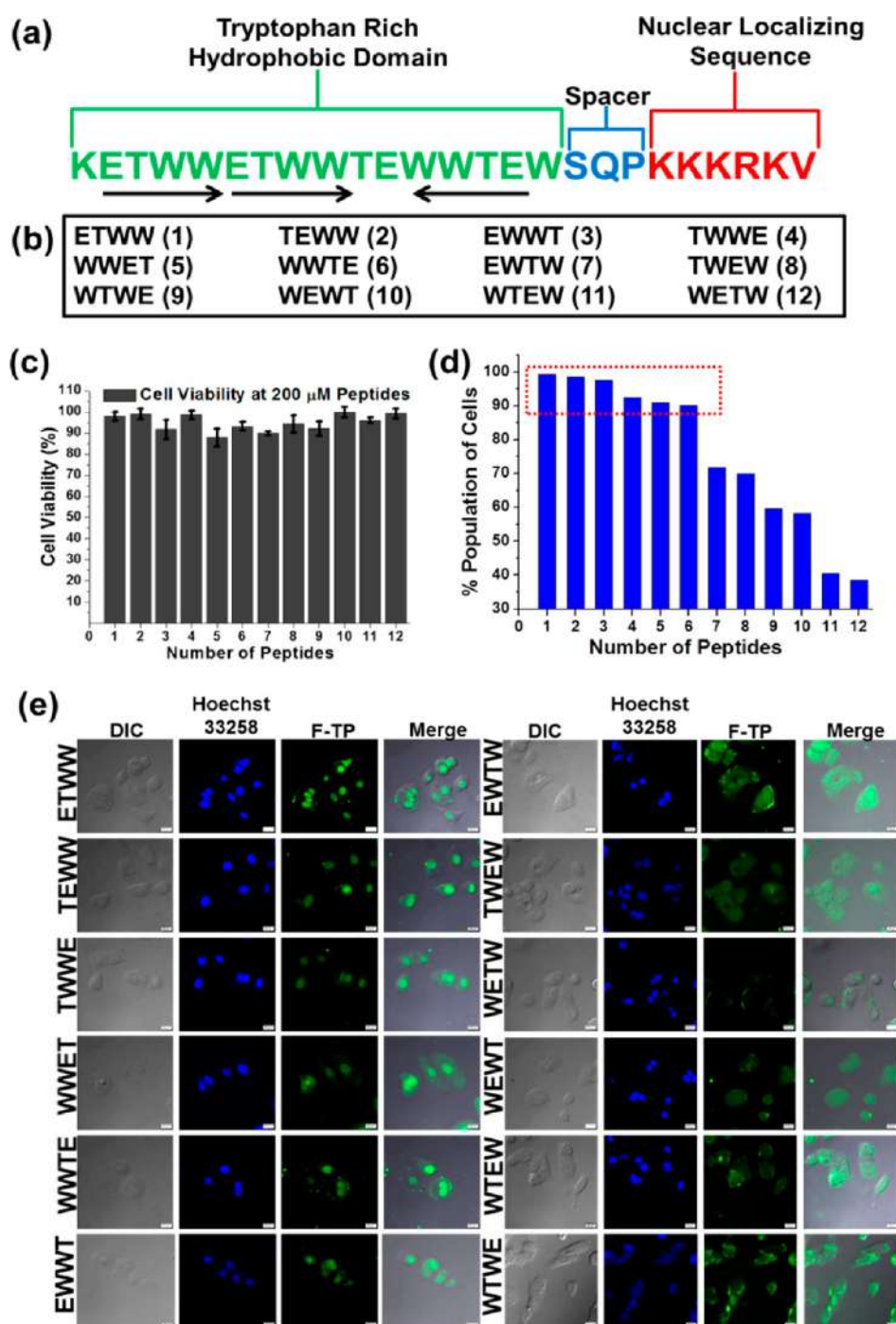
Figure 1. (a) Amino acid sequence of Pep1 peptide, revealing repetitive ETWW/WWTE tetrapeptide sequence. Arrows indicate N- and C-terminal directions for designing the tetrapeptide library. (b) Library consisting of 12 tetrapeptide sequences, designed by changing the position of tryptophan, named as **1−12**. (c) Human breast cancer cell (MCF7) viability assay of the 12 tetrapeptides at 200 μM concentration, showing the non-cytotoxic nature of all 12 tetrapeptides. Error bars represent standard error of the value. (d) Cellular uptake of all the fluorescein-tagged tetrapeptides having 5 μM concentration studied by FACS, revealing quantitative uptake of tetrapeptide **1−6** are maximum and gradually decreases from **7−12** into the MCF7 cells. Tetrapeptides **11** and **12** show poor uptake into the MCF7 cells. (e) Cellular uptake of fluorescein-tagged tetrapeptides. Microscopic images are shown for cells captured in DIC mode, 405 and 488 nm channels. The column at the extreme right for both panels shows merged images of DIC mode and 488 nm. Images from tetrapeptides **1−6** reveal clear localization of tetrapeptides in the nucleus of MCF7 cells, while tetrapeptides **7−12** show penetration into the MCF7 cell without localization in the nucleus. Scale bars correspond to 20 μm.

CPPs? To address this question, it is highly important to identify the minimum sequences necessary for successful cellular entry and to understand the mechanistic aspects of cell penetration. We observed that "Chariot" contains a repetitive "ETWW" (Glu-Thr-Trp-Trp) tetrapeptide sequence.

However, the exact role of this repetitive unit was not explored yet. Thus, in the work described in this Article, we tried to understand the exact role of this tetrapeptide along with the specificity of tryptophan in translocation.

First, a small library of 12 tetrapeptides was constructed by changing the position of tryptophan in ETWW (Figure 1b), and their cell viability, cellular entry, nuclear localization, and DNA binding efficiency were studied (Figure 1c,d). Intriguingly, we found that six tetrapeptides consisting of a trp-trp sequence demonstrated excellent cellular penetration, cell viability, nuclear localization, and strong interaction with double-stranded DNA (dsDNA) on a two-dimensional (2D) micropatterned surface. In contrast, when a spacer amino acid—either Glu (E) or Thr (T)—was incorporated between the trp-trp sequence in six other tetrapeptides, their cellular uptake, cell viability, nuclear localization, and interaction with DNA were all insignificant. This result clearly indicates that the trp-trp sequence plays a crucial role. Among the six tetrapeptides containing the trp-trp sequence, we found that ETWW has the maximum beneficial effect on cellular penetration, cell viability, nuclear localization, and interactions with dsDNA. Further, we found that ETWW enters into the cell through an endocytosis mechanism, and its interaction with nuclear DNA was observed even in the metaphase stage of cell division. More importantly we explored the excellent cell penetration and nuclear localization capabilities of ETWW and demonstrated its capability to penetrate into a stem-cell-like multi-cellular three-dimensional (3D) cell culture system. Finally, the excellent effect of ETWW tetrapeptide in cell penetration and nuclear localization was further utilized for the development of a nucleus-targeting drug delivery vehicle and evaluated in 3D cell culture as well as in *in vivo* mice melanoma model. Moreover, substitution of Glu (E) or Thr (T) in the ETWW sequence with Asp (D) or Ser (S) showed results similar to those observed in peptides containing successive trp-trp. This study further strengthens the significance of successive trp-trp in cell penetration, nuclear localization, and interaction of dsDNA.

2. EXPERIMENTAL SECTION

2.1. Materials. All Fmoc-protected amino acids and Wang resin were purchased from Novabiochem (Merck). N,N-Dimethylformamide (DMF), dichloromethane (DCM), diethyl ether, trifluoroacetic acid (TFA), piperidine, O-(benzotriazol-1-yl)-N,N,N′,N′-tetramethyluronium hexafluorophosphate (HBTU), diisopropylethylamine (DIEA), dimethyl sulfoxide (DMSO), and methanol were purchased from Spectrochem. Ethanedithiol (EDT) and phenol were bought from Merck. 5,6-Carboxyfluorescein, guanosine-5′-triphosphate sodium salt hydrate (GTP), β-casein, catalase, glucose oxidase, 3-(4,5-dimethylthiazol-2-yl)-2,5-diphenyltetrazolium bromide (MTT), Dulbecco's modified eagle medium (DMEM), kanamycin sulfate, trypsin-EDTA solution, DMSO for cell culture, and formaldehyde solution for molecular biology were bought from Sigma-Aldrich. (3-Glycidoxypropyl)trimethoxysilane (GOPTS), N,N′-diisopropylcarbodiimide (DIC), and NGF Beta-7S were also purchased from Sigma-Aldrich. Penicillin—streptomycin, neutravidin, fetal bovine serum (FBS), and Cy3.5 (Alexa Fluor 555) were purchased from Invitrogen. Annexin V-FITC and propidium iodide apoptosis detection kit were bought from Santa Cruz Biotechnology. Bisbenzimide H 33258 (Hoechst) was purchased from Calbiochem. Covered glass-bottom dishes were purchased from SPL. Single-stranded oligonucleotide sequences (ssDNA; ssDNA1 = 5′-GCGC-ATGCTACGCG-3′ and ssDNA2 = 5′-CGCGTAGCATGCGC-3′), biotin, and TRITC-labeled ssDNA were procured from Eurofins India Pvt Ltd. Other different AT (%)- and GC (%)-containing DNA duplexes (Supporting Information (SI)) were also purchased from Eurofins India Pvt Ltd. Anti-Eg5 primary antibody was purchased from Abcam. Horse serum was bought from Himedia. These compounds were used without further purification. For peptide purification, we used a Shimadzu high-performance liquid chromatography (HPLC)

system with a C-18 reverse-phase column. Water used for experiments was of Milli-Q grade. HPLC-grade acetonitrile was purchased from J.T. Baker. An Olympus IX83 fluorescence microscope was used for cell imaging. Synthesized peptide masses were confirmed by matrix-assisted laser desorption/ionization time-of-flight mass spectrometry (MALDI-TOF-MS). Healthy black mice (C57BL6J) were bought from NIN, Hyderabad.

2.2. Cell Culture. Different types of cell lines—MCF7, HeLa, A549, U87, HepG2, and B16F10—were purchased from the National Centre for Cell Science (NCCS) Pune, India. Cells were cultured in 5% CO_2 in an incubator at 37 °C using DMEM containing FBS (10%), kanamycin sulfate (110 mg/L), penicillin (50 units/mL), and streptomycin (50 μg/mL) in our laboratory. Trypsin-EDTA (1X) solution was used for cell detachment during cell splitting. PC12 cells (kind gift from Dr. Suvendra N. Bhattacharyya) were cultured in DMEM containing FBS (5%), horse serum (10%), kanamycin sulfate (110 mg/L), penicillin (50 units/mL), and streptomycin (50 μg/mL) in our laboratory.

2.3. Synthesis of Tetrapeptides and Fluorescein-Attached Tetrapeptide Analogues. All the tetrapeptides and their fluorescent analogues were synthesized by the solid-phase peptide synthesis (SPPS) method. 5(6)-Carboxyfluorescein dye was covalently attached with the tetrapeptides using SPPS. Tetrapeptides and fluorescein-tagged tetrapeptides were purified by C-18 reverse-phase HPLC, and masses were confirmed by MALDI-MS (SI).

2.4. Cell Viability Study. Cell viability assays of all tetrapeptides were performed up to 200 μM concentration following the standard procedure (SI). Cell viability was checked in MCF7, HeLa, A549, U87, HepG2, and B16F10 cells. The percentage viability was calculated from absorbance values as $[(A_{550}(\text{treated cells}) - A_{550}(\text{backgrounds}))/(A_{550}(\text{untreated cells}) - A_{550}(\text{backgrounds}))] \times 100$. Similarly, cell viability of LLCPD (liposome embedded with long chain attached ETWW peptide containing doxorubicin)-treated samples was checked in MCF7 as well as B16F10 cells.

2.5. Docking Study. Autodock-Vina software version 1.1.2 was used for blind docking using a grid box volume of 98 × 60 × 64, centered on the receptor GG28 DNA (PDB ID: 2M2C) for docking with ETWW tetrapeptide (SI).

2.6. Nuclear Localization Monitored by Microscopic Imaging. Cellular uptake of all fluorescein-attached tetrapeptides was studied in human breast cancer MCF7 cells after 4 h incubation at 37 °C. The nucleus was stained with Hoechst 33258 (1 μg/mL) for 1 h. After complete washing with phosphate-buffered saline (PBS), imaging was performed on an Andor spinning disc confocal microscope with a 40× objective (Olympus), equipped with an Andor iXon3 897 electron-multiplying charge-coupled device (EMCCD) camera in bright field, 488 and 405 nm channels (SI).

2.7. Pathway Involved in Cellular Internalization of ETWW. Cellular internalization of fluorescein-tagged ETWW (F-ETWW, 5 μM) was analyzed for 4 h. Cells were then incubated at 37 or 4 °C for 50 min separately. Next, cells were treated with 5 μM F-ETWW and incubated at 37 or 4 °C for 4 h separately. After complete wash with colorless media and centrifugation, cells were washed with serum-free DMEM (colorless) culture medium, and the fluorescent signal was analyzed using with the 488 nm channel of a BD LSRFortessa flow cytometer using an emission filter at 530 nm.

2.8. Interaction of ETWW with Key Cell Surface Receptors Responsible for Cellular Uptake and Efflux of Drug Using Molecular Docking Technique. Autodock version 1.1.2 was used to dock ETWW peptide with different cell receptors.

Endothelin Receptor. We performed blind docking of ETWW peptide with endothelin receptor (PDB ID: 5GLH). The grid box of 68 × 100 × 74 was centered on the receptor. It shows significant binding of ETWW peptide with this receptor (binding energy −8.1 kcal/mol). The −NH group (−CONH) of TRP 3 with the −OH group of CYS 15 (receptor), and the −NH group (indole ring) of TRP 3 with the >C=O group of TYR 369, are in H-bonding interactions. The acid group (−COOH) of TRP 4 is in H-bonding interaction with −NH$_2$ of LYS 182 and LYS 273 (SI). Also, the interactions are further

stabilized by H-bonding and hydrophobic interactions between different amino acids.

Opioid Receptor. We performed blind docking of ETWW peptide with mu opioid receptor (PDB ID: 4DKL). The grid box of 52 × 98 × 66 was centered on the receptor. The binding energy (−8.1 kcal/mol) shows good binding of ETWW peptide with the opioid receptor. The −OH group of TYR 148 with the −NH group (indole ring) of TRP 3, the >C=O group (−CONH) of GLN 124 with the −NH group (indole ring) of TRP 4, and the >C=O group of TRP 4 (−COOH) with the −NH group (indole ring) of TRP 318 are in H-bonding interactions.

P-glycoprotein (P-gp) Receptor. For the docking with P-glycoprotein (P-gp) receptor, we used PDB structure 3G5U from the RCSB Protein Data Bank. The grid box of 66 × 70 × 74 was centered on the receptor drug binding site. After analyzing the binding site of this peptide, we found that this peptide is not at all binding to any binding site (i.e., M site, R site, H site); rather it has affinity for binding to the outer surface of the receptor. The details of the interactions are given in the SI.

Moreover, we performed endothelin, opioid, and P-gp receptor binding studies with WTWE and WETW, where the two tryptophan units are not close to each other, following the methods described above. Details of the interactions are given in the SI.

2.9. Flow-Cytometry-Based Comparative Cellular Uptake Kinetics Study of F-ETWW and Doxorubicin (DOX, a Known P-gp Substrate). A time-dependent cellular uptake study was performed by flow cytometry using 5 μM F-ETWW and 2 μM doxorubicin (DOX) in MCF7 cells. First, MCF7 cells were harvested at 37 °C in an incubator prior to treatment for 24 h. MCF7 cells were then treated with either as DOX or F-ETWW for increasing incubation times (30 min, 2 h, 4 h, and 6 h) in serum-free colorless media. After that, cells were centrifuged, and cellular uptake of both DOX and F-ETWW was recorded as fluorescence intensity and analyzed by fluorescence-assisted cell sorting (FACS; Ex-488 nm and Em-500 to 600 nm for F-ETWW, and Ex-560 nm and Em-580 to 700 nm for DOX).

2.10. Immunostaining Study with Eg5. MCF7 cells having a cell density of 5000 cells were harvested on a glass-bottom dish overnight. After that, cells were treated with 5 μM F-ETWW for 4 h at 37 °C in 5% CO$_2$. Next, the cells were fixed with 4% formaldehyde for 1 h and incubated with 0.2% Triton-X and 5% BSA in PBS for 1 h. After a single wash with 1× PBS, cells were incubated with polyclonal anti-Eg5 IgG antibody with dilution 1:300 overnight at 4 °C. Cells were then washed with PBS and incubated with secondary antibody (Cy3 pre-absorbed goat anti-mouse IgG) with dilution 1:600 for 2 h at 37 °C. Again the cells were washed with 1× PBS, followed by incubation with Hoechst 33258 (1 μg/mL) for 30 min before imaging. Images were captured from a confocal microscope using a 40× objective (Olympus), equipped with an Andor iXon3 897 EMCCD camera, in 405, 488, and 561 nm wavelength laser lights.

2.11. Monitoring Interaction between Fluorescein-Tagged Tetrapeptide and Double-Stranded DNA (dsDNA) on 2D Biotin Micropatterned Surface. Square-shaped biotin micropatterned surfaces were generated using a photomask and UV light as described previously.[32] A flow chamber was made with a micropatterned glass surface and poly-L-lysine−poly(ethylene glycol) passivated counter glass and equilibrated for 7 min with β-casein solution (1 mg/mL) in HEPES buffer. Next, the flow chamber was incubated with a solution of neutravidin (300 nM) in HEPES buffer for 7 min. Excess neutravidin was washed out by HEPES buffer, and after that a 30 μM solution of the biotin-tagged TRITC-dsDNA was loaded into the flow chamber and incubated for 10 min. Excess dsDNA was washed out by HEPES buffer. Finally, 20 μL solutions of fluorescein-tagged tetrapeptides (10 μM) in HEPES buffer were loaded into the flow chamber and incubated for 10 min (SI), followed by washing with HEPES buffer to remove excess fluorescein-tagged tetrapeptides. Images were captured under fluorescence microscope at 488 and 561 nm wavelengths.

2.12. Förster Resonance Energy Transfer (FRET) Study. FRET is the study of non-radiative energy transfer from an excited donor

molecule to a ground-state acceptor molecule. A FRET pair is chosen by measuring a significant overlap region. We performed a FRET study between F-ETWW peptide and TRITC-dsDNA. From this FRET study, we measured the distance between them, which is 72 ± 2 Å (SI).

2.13. Determination of Interaction Site of ETWW at dsDNA. All absorbance spectra were measured on a UV spectrophotometer at 25 °C in 20 mM phosphate buffer (pH 7.2), containing 1 mM EDTA and 50 mM NaCl. In order to understand whether ETWW tetrapeptide binds to the major groove of dsDNA independent of sequence context, we performed Methyl Green displacement experiments using UV−visible spectroscopy, since Methyl Green is a well-known major-groove-binding dye. We used eight different oligonucleotide sequences with different AT and GC contents (Table T1) and mixed Methyl Green with the sequences in a 1:1 molar ratio. We checked their absorption spectra in the range of 500−700 nm. The change in the absorption spectrum at the λ_{max} of the dye (632 nm) was monitored with each successive addition of ETWW. We then plotted the absorption values of Methyl Green against various peptide concentrations. Similarly, a minor-groove-binding fluorescent dye, 4′,6-diamidino-2-phenylindole (DAPI), which selectively binds the AT-rich minor groove of dsDNA, was used to determine whether the peptide binds to the minor groove of dsDNA. The excitation wavelength was 372 nm, and the emission profile was monitored from 400 to 520 nm.

The binding affinity of ETWW with various oligonucleotide sequences having different AT and GC contents and distribution was estimated by gradually titrating the oligonucleotides with 10 μM ETWW peptide. The quenching of tryptophan fluorescence intensity is plotted against increasing concentration of DNA, and the quenching constant was calculated using the Stern−Volmer equation (SI).

2.14. 1D and 2D Nuclear Magnetic Resonance (NMR) Study. Exchangeable and non-exchangeable protons of dsDNA were observed in the 1D ^{1}H NMR spectra under free and ETWW-bound conditions using Bruker Pulprog "zgesgp" with a spectral width (sw) of 20 ppm, number of scans (ns) of 512, and calibrated pulse length (pl) of 12.48 μs (SI). T1 and T2 relaxation experiments were performed to study the dynamics of the exchangeable protons at free and peptide-bound conditions using inversion recovery delay and CPMG refocusing, respectively. 2D ^{1}H−^{1}H nuclear Overhauser effect spectroscopy (NOESY) of the peptide−DNA complex were collected in 90% H$_2$O and 10% D$_2$O using Bruker's "noesyesgpph" pulse program with a mixing time of 300 ms.

2.15. Watergate NOESY. Watergate NOESY spectra were acquired on a 700 MHz Bruker Avance spectrophotometer at 15 °C under free and ETWW-bound conditions. We used the standard pulse sequence "noesygpph19" in the Bruker sequence library, with water suppression using a Watergate 3-9-19 sequence with gradients. The mixing times were set at 50, 70, 100, and 150 ms. Relaxation delay was 1.5 s. The spectra were processed in Bruker TOPSPIN 3.1. After Fourier transformation, the spectra were phase corrected and calibrated to the TSP signal at 0 ppm.

2.16. Generation of Stem-Cell-Like Multi-cellular 3D (Spheroid) Cell Culture of Mice Melanoma Cells. For evaluation of the penetration ability of ETWW into the spheroid, stem-cell-like multi-cellular 3D (spheroid) cell culture was established for B16F10 cells. Cells were cultured on 35 mm round-bottom cover disks previously coated with 1% agarose. Cells were then treated with F-ETWW peptide for 4 h, followed by Hoechst 33258 treatment for 1 h. Co-localization images were observed between F-ETWW and Hoechst. Spheroids were monitored under a fluorescence microscope in DIC mode, 405, and 488 nm wavelengths.

2.17. Preparation of ETWW Lipopeptide. Lipopeptide was synthesized by reacting 2 equiv of 1-bromohexadecane with 1 equiv of mono-boc ethylenediamine for 48 h under reflux conditions. After synthesis of C16-ETWW, lipopeptide was purified by C-18 column reverse-phase HPLC and characterized by MALDI-TOF-MS (SI).

2.18. Preparation of ETWW-Embedded Liposome and Encapsulation of DOX. We prepared liposome containing C16-ETWW lipopeptide using the hydration method and encapsulated

DOX inside the liposome as previously described.[49] In brief, 1,2-dioleoyl-sn-glycero-3-phosphocholine (DOPC), cholesterol, and C16-ETWW were mixed together, followed by lyophilization for 2 h. DOX was dissolved in 5 mL of 5% glucose solution (w/v) and then incubated for 2 h with the liposomes at 37 °C for proper entrapment. DOX concentration was determined by absorbance measurement of liposome at 480 nm (SI). LLCPD was characterized by dynamic light scattering (DLS) and cryo-electron microscopy (cryo-EM).

2.19. Growth Inhibition Study of Stem-Cell-Like Multi-cellular 3D (Spheroid) Cell Culture. Stem-cell-like multi-cellular 3D (spheroid) cell cultures were established for both MCF7 and B16F10 cells. Cells were cultured on 35 mm round-bottom cover disks previously coated with 1% agarose. Cells were then treated with LLCPD along with control liposome and DOX alone. Sizes of spheroids were monitored under a microscope.

2.20. In Vivo Study. C57BL/6J female mice having average body weight of 15−17 g were chosen for *in vivo* study. Initially, mice melanoma B16F10 cells in PBS were injected, and after growth of tumors of average volume 1000 mm³, the mice were randomly divided into two groups (5 mice/group), i.e., treated and untreated (group 1 and group 2, respectively). LLCPD ([DOX] = 5 mg/kg) was administered on the first and eighth days for group 1, whereas group 2 remained untreated. Tumor volume and mice body weight were measured from 0 to 14 days. Mice were sacrificed by cervical dislocation, and tumors were collected and their sizes measured. Haematoxylin and eosin (H&E) staining was performed for histological study (SI).

2.21. Effect of ETWW on PC12-Derived Neurons: Cell Viability and Microscopic Imaging Using PC12-Derived Neurons. PC12 cells were seeded on 96-well plates and 35 mm glass-bottom dishes overnight. Cells were then differentiated using 100 ng/mL NGF mouse protein in serum-free medium for 5 days. After PC12 cells completely differentiated into mature neurons, they were treated with ETWW at various concentrations (200, 100, 50, 25, 12.5, 6.25, 3.125, and 1.56 μM) and incubated for 24 h at 37 °C in 5% CO$_2$. Following the incubation, 5 mg/mL of MTT solution was added to each well of the 96-well plate and incubated for 4 h. The medium was removed, and DMSO−MeOH (1:1) was used to solubilize formazan prior to reading. The 96-well plates were then scanned using a microplate ELISA reader (Thermo, Multiscan GO microplate spectrophotometer) at a wavelength of 550 nm. Similarly, the PC12-derived neurons seeded on 35 mm dishes were divided into two sets. The first one was treated with ETWW at an optimum concentration of 50 μM, and the other one remained untreated (control) for 24 h after differentiation. Following incubation, the neurons were imaged under a confocal fluorescence microscope (Olympus IX83 microscope equipped with an Andor iXon3 897 EMCCD camera) in DIC mode.

3. RESULTS

3.1. Design and Synthesis of Tetrapeptide Library, Its Cell Viability, and Cellular Uptake by Fluorescence-Assisted Cell Sorting (FACS) Technique. A small library of 12 tetrapeptides was constructed by shifting the position of amino acids (Figure 1b and SI). Moreover, ESWW and DTWW were designed by exchanging T and E with S and D, respectively, as control tetrapeptides. All the tetrapeptides were synthesized using SPPS method, purified by HPLC on a C-18 reverse-phase column, and characterized by MALDI-MS (Figures S1−S14). Similarly, all the tetrapeptides were covalently attached with fluorescein using SPPS method for studying the cellular entry and nuclear localization (Figures S15−S28).

The toxicity of all the synthesized tetrapeptides was evaluated through cell viability assay, which was performed in human breast cancer cells (MCF7) in an atmosphere of 5% CO$_2$ at 37 °C using DMEM upon treatment of peptides up to 200 μM concentration for 24 h (Figures 1c, S29, and S30). Cell viability study revealed that all the tetrapeptides are non-cytotoxic in

nature. Next, we quantitatively checked the efficiency of cellular entry of 12 tetrapeptides in MCF7 cells using flow cytometry. Cells were treated with fluorescein-tagged tetrapeptides for 4 h (SI). Interestingly, FACS results for all the tetrapeptides revealed that those containing successive tryptophan showed better uptake in comparison to peptides containing non-successive tryptophan, indicating that the trp-trp sequence in the tetrapeptides facilitates cellular entry. Further, we observed that uptake of F-ETWW is highest compared to all the other tetrapeptides (Figures 1d, S31, and S32).

3.2. Evaluation of Cellular Uptake of Fluorescein-Tagged Tetrapeptides inside the MCF7 Cells Using Fluorescence Microscopy. Next, cellular uptake of all tetrapeptides was checked using fluorescence microscopy. MCF7 cells were treated with fluorescein-tagged tetrapeptides and incubated for 4 h. Cell nucleus was stained with Hoechst 33258 and incubated for 1 h. Images were captured at DIC mode, 405 and 488 nm channels. Fluorescence microscopy images revealed that tetrapeptides containing successive tryptophan successfully entered into the cells and localized preferentially at the nucleus; i.e., green-colored tetrapeptides co-localized with the nucleus of MCF7 cells. Most interestingly, we observed that peptides containing successive tryptophan strongly localized in the nucleus even in the presence of minor-groove-binding dye Hoechst 33258.[30] This result clearly indicates that tetrapeptides containing successive tryptophan may have different binding sites other than the minor groove of DNA in the nucleus. However, further experiments are required to confirm this observation. In contrast, we observed low cellular uptake of tetrapeptides containing non-successive tryptophan, mostly present in the cytoplasm without localization in the nucleus (Figures 1e and S33). Among all the tetrapeptides, ETWW showed excellent localization in the nucleus and elevated cellular uptake in the MCF7 cells, which confirms that it is the tetrapeptide with greatest potential in our peptide library (Figures 1 and S15−S28). Thus, taking these leads, we preceded further with experiments using this tetrapeptide. However, other tetrapeptides containing successive tryptophan showed good potential and could be explored in follow-up work.

3.3. Evaluation of ETWW Cell Viability in Various Cancer Cell Lines. Before performing detailed studies of ETWW, we studied the cell viability of ETWW in various cancer cell lines such as human epitheloid cervix carcinoma (HeLa), human lung carcinoma (A549), human glioblastoma (U-87 MG), and human liver hepatocellular carcinoma (HepG2). Results indicate the non-toxic nature of ETWW (Figure S34).

3.4. Interaction of Tetrapeptides with dsDNA Monitored Using 2D Micropatterned Surface. Excellent nuclear localization of tetrapeptides containing trp-trp sequence indicates that they can efficiently interact with DNA, as the nucleus contains a high amount of chromatin DNA. Now, this evokes curiosity about how these tetrapeptides interact with DNA and whether the position of tryptophan plays a pivotal role. To address these questions, we performed various assays choosing a small dsDNA and biotinylated TRITC-labeled dsDNA (Scheme Sc1).[31] As the first experiment we used our previously developed surface chemistry assay,[32] where we prepared a neutravidin-immobilized 2D biotin micropatterned surface for selective immobilization of biotinylated TRITC-dsDNA. Subsequently, all the fluorescein-tagged tetrapeptides and two control tetrapeptides were incubated for 10 min,
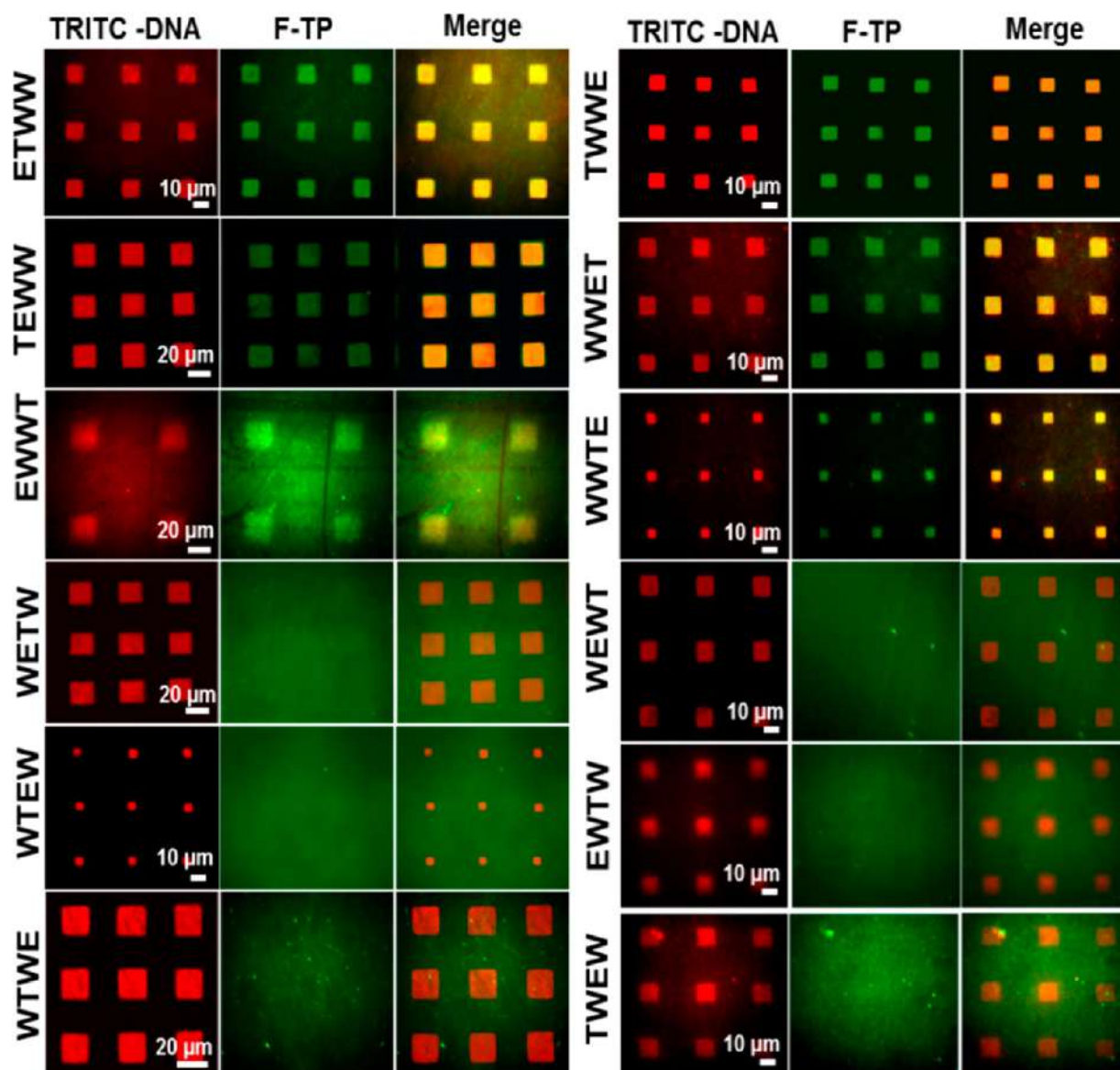
Figure 2. 2D micropatterned assay for studying interaction between fluorescein-tagged tetrapeptides and Biotin-TRITC-dsDNA. Fluorescein-tagged tetrapeptides were incubated in a flow chamber containing immobilized Biotin-TRITC-dsDNA on a square-shaped neutravidin−biotin-micropatterned surface, followed by washing of excess and unbound fluorescein-tagged tetrapeptides. Images were captured at 488 and 561 nm channels. Images of fluorescein-tagged tetrapeptides **1−6** reveal that tetrapeptides bind with dsDNA, as we observe yellow-colored square-shaped micropatterns in merged images. But the yellow-colored square-shaped micropatterns were not observed in the case of fluorescein-tagged tetrapeptides **7−12**, indicating that tetrapeptides **7−12** did not interact with dsDNA. These results clearly indicate that trp-trp in tetrapeptides **1−6** plays a crucial role in their interaction with dsDNA.

followed by repeated washing to remove unbound tetrapeptides (SI). The 2D micropatterned surfaces were observed under a fluorescence microscope at 488 and 561 nm wavelengths, followed by capturing images using an EMCCD camera. Fluorescence microscopy images revealed excellent co-localization of fluorescein-tagged tetrapeptides containing successive tryptophan with TRITC-labeled dsDNA, whereas we did not observe any co-localization of fluorescein-tagged tetrapeptides containing non-successive tryptophan on 2D micropatterned surfaces, indicating the significant role of the two-successive-tryptophans unit in the interaction with dsDNA (Figures 2 and S35). This assay also shows that ETWW tetrapeptide interacts with dsDNA strongly on a 2D micropatterned surface, along with other tetrapeptides containing the trp-trp sequence.

Therefore, these observations support the specific co-localization of tetrapeptides with the nucleus of MCF7 cells.

3.5. Mechanistic Pathway Involved during Uptake of ETWW Monitored by Flow Cytometry and Computational Analyses. Further, we tried to understand the mechanistic pathways involved during cellular uptake of ETWW tetrapeptide by flow cytometry. For that purpose, two sets of cultured cells were treated with F-ETWW and incubated at 37 or 4 °C for 4 h separately. FACS data revealed that uptake of F-ETWW into the MCF7 cells incubated at 37 °C is higher compared to that at 4 °C. This result clearly indicates that cellular uptake of ETWW tetrapeptide follows the endocytosis mechanism (Figure 3a and SI).

Cellular endocytosis of ETWW encourages us to find the possible cell surface receptor involved in internalization
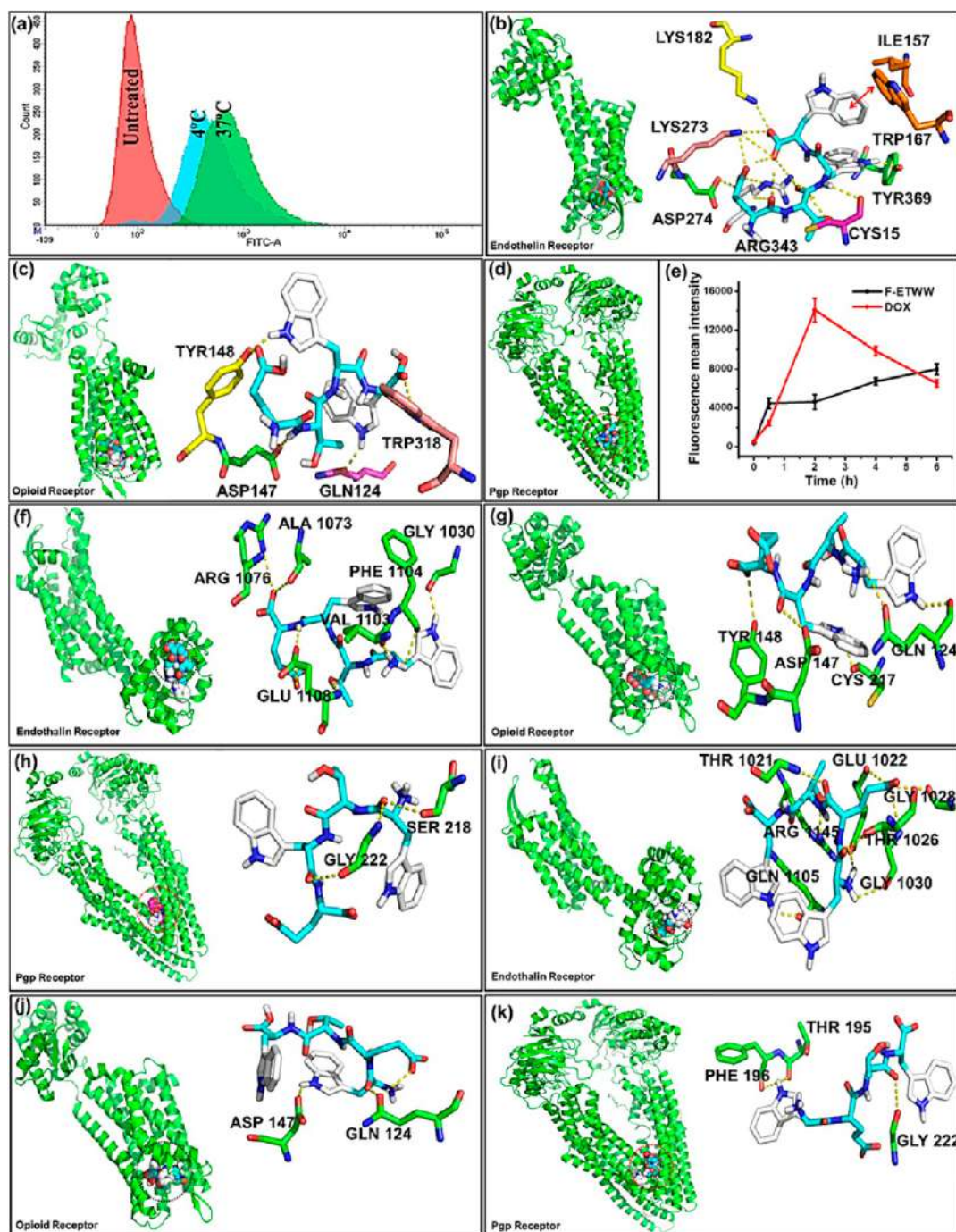
Figure 3. Insights into cellular entry of ETWW through interactions with key receptors at the cell membrane. (a) Cellular uptake study of 5 μM F-ETWW indicates that uptake follows an endocytosis mechanism. Molecular docking study of ETWW peptide with (b) endothelin receptor and (c) opioid receptor shows significant interactions with both the receptors responsible for the endocytosis mechanism. Further docking images reveal that both tryptophans in ETWW play crucial roles in interactions with the receptor. Computational and flow-cytometry experiments reveal that ETWW is not a P-gp substrate, indicating its potential as a CPP. (d) Docking study with ETWW and P-glycoprotein receptor shows that ETWW binds at the outer surface of a P-gp receptor without interacting with its known binding pockets (R, H, and M). (e) Flow cytometry-based cellular uptake kinetics study in MCF7 of F-ETWW and DOX (known P-gp substrate) reveals that uptake of ETWW increases with time, indicating no efflux of ETWW, while uptake of DOX significantly decreases after 2 h, indicating efflux of DOX. Error bars represent standard error of the value. Molecular docking studies of WTWE and WETW with (f,i) endothelin receptor, (g,j) opioid receptor, and (h,k) P-gp receptor.

pathway. Thus, we adopted a computational virtual screening (VS) tool using ligand-based (LBVS) and structure/receptor (SBVS)-based techniques. We used the "SwissSimilarity" online tool (http://www.swisssimilarity.ch), which offers LBVS with six different methods on >30 chemical databases.[33] Here, we analyzed the similarity of ETWW with a ligand database.

Initially, we performed the "SwissTargetPrediction" method (http://www.swisstargetprediction.ch) to screen possible target receptors of ETWW based on ligand similarity search.[34] Intriguingly, we observed that ETWW shows both 2D- and 3D-based structural similarity with various ligands of two important cell membrane receptors with significant probability,
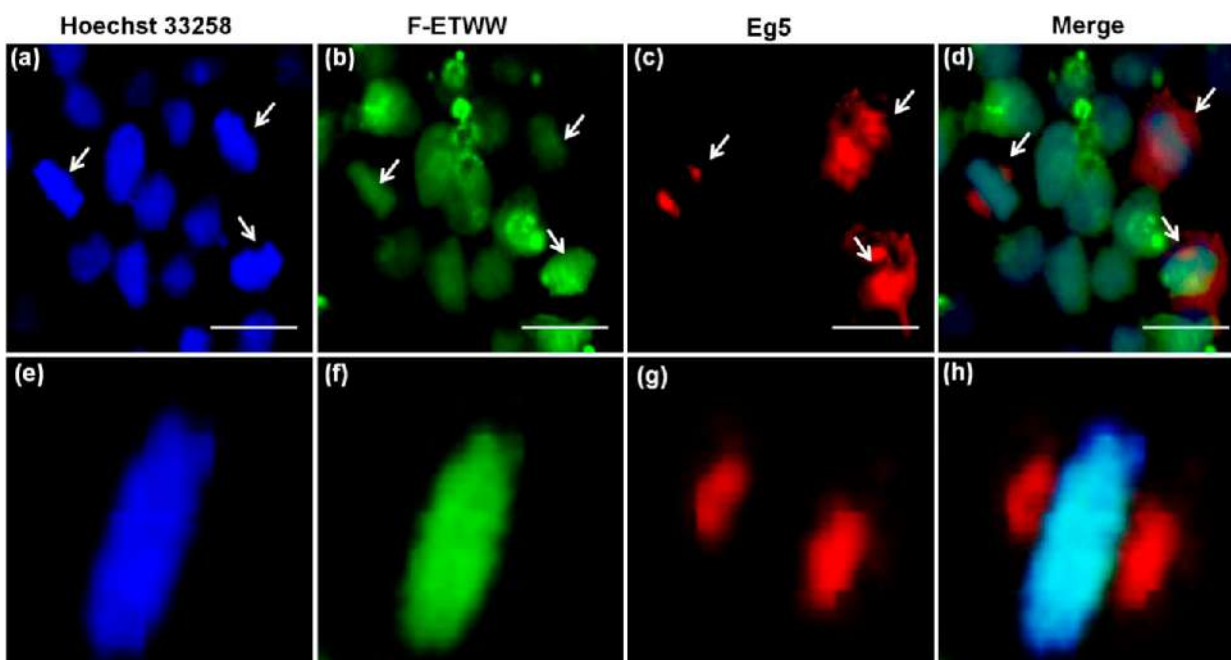
Figure 4. Interaction of ETWW with chromatin DNA in metaphase plate using kinesin 5 (Eg5) assay. (a) Chromatin DNA stained with Hoechst 33258, (b) F-ETWW, (c) Eg5 immunostained with anti-mouse Eg5, and (d) co-localized image of the three channels, revealing that ETWW retains its nuclear binding ability with the condensed chromatids even in the absence of nuclear envelope (metaphase plate), which is the mitotic check point, a crucial target for drug design. Arrows indicate the cells at metaphase stage (dividing) among the non-dividing cells. (e−h) Zoomed-in images reveal better resolution of the interactions between ETWW and chromatid. Scale bars correspond to 20 μm.

named endothelin B (ETB), and mu opioid receptors and also found similarity to various surface antigens. On the basis of endocytosis, we postulated two membrane receptors for cellular internalization study. Thus, we adopted a receptor-based technique using a molecular docking method and scoring method to analyze ligand−receptor interactions. Here, we performed docking using ETWW peptide as ligand and either ETB or mu opioid membrane proteins as receptor. Docking with ETB receptor reveals significant polar and non-polar interactions of this peptide with higher scoring value (binding energy −8.1 kcal mol^{-1}) (Figure 3b and SI). Briefly, polar or H-bonding interactions include >C=O moieties (−COOH) of ASP 274 and ARG 343 (receptor) with the −OH group (−COOH) of GLU 1 of the peptide, the −NH group (−CONH) of TRP 3 with the −OH group of CYS15 of the receptor, the −NH group (indole ring) of TRP 3 (peptide) with the >C=O group of TYR 369 (receptor), and the −COOH group of TRP 4 (peptide) with −NH$_2$ of LYS 182 and LYS 273 (receptor). The interaction is further stabilized by hydrophobic interaction between ILE 157 and TRP 167 (receptor) with TRP 4 (peptide). Interestingly, the interactions are similar to the previously described interactions found between ETB receptor and its peptide ligand, termed endothelin-1.[35] These findings reveal that ETWW peptide interacts with a known ligand-binding pocket of ETB receptor, where two successive tryptophans play an important role.

We also performed molecular docking of the peptide with the mu opioid receptor. The binding energy (−8.1 kcal mol^{-1}) reveals good binding of this peptide with the receptor (Figure 3c and SI). The −OH group of TYR 148 (receptor) with the −NH group (indole ring) of TRP 3 (peptide), the >C=O group (−COOH) of ASP 147 (receptor) with the −NH (−CONH) group of THR 2 (peptide), the >C=O group (−CONH) of GLN 124 (receptor) with the −NH group

(indole ring) of TRP 4 (peptide), and the >C=O group of TRP 4 (−COOH) (peptide) with the −NH group (indole ring) of TRP 318 (receptor) are in H-bonding interactions. These interactions are observed at the known binding pocket of the mu opioid receptor, supporting the fact that ETWW interacts with crucial amino acids of the mu opioid receptor responsible for the endocytosis process.[36] Further, we would like to mention here that the two successive tryptophans play important roles, as we observed both interacting in the pocket through H-bonding.

Although receptor-mediated endocytosis uptake is a vital cellular internalization process, cellular availability of the molecule is not only proportional to its membrane receptor but also inversely related to multi-drug resistance (MDR) protein or P-glycoprotein (P-gp). This ABC transporter is over-expressed in various cancer cells and impairs chemotherapy due to its broad specificity toward many substrate molecules, including both polar and non-polar amphipathic molecules and several peptides.[37] Thus, intracellular concentration of various indispensable anticancer drugs like doxorubicin, paclitaxel, vinblastine, etopside, and daunorubicin gets impaired. The role of P-gp-mediated efflux is also not limited to exogenous substances; rather, it can also modulate the distribution of endogenous substances such as endogenous opioid peptides.[38] Therefore, it was obvious to analyze the ETWW peptide interaction with P-gp receptor. Initially the "SwissADME" method was implemented (http://www.swissadme.ch), and we observed non-specificity of ETWW with P-gp and various CYPs (cytochrome 450, involved in drug deactivation). This result inspired us to seek a structure-based understanding of the possible interactions. Hence, molecular docking was performed between ETWW and the crystallographically well-characterized P-gp receptor.[39,40] ETWW peptide does not bind to any of the reported binding sites (i.e., M, R, and H sites);[40] rather it has
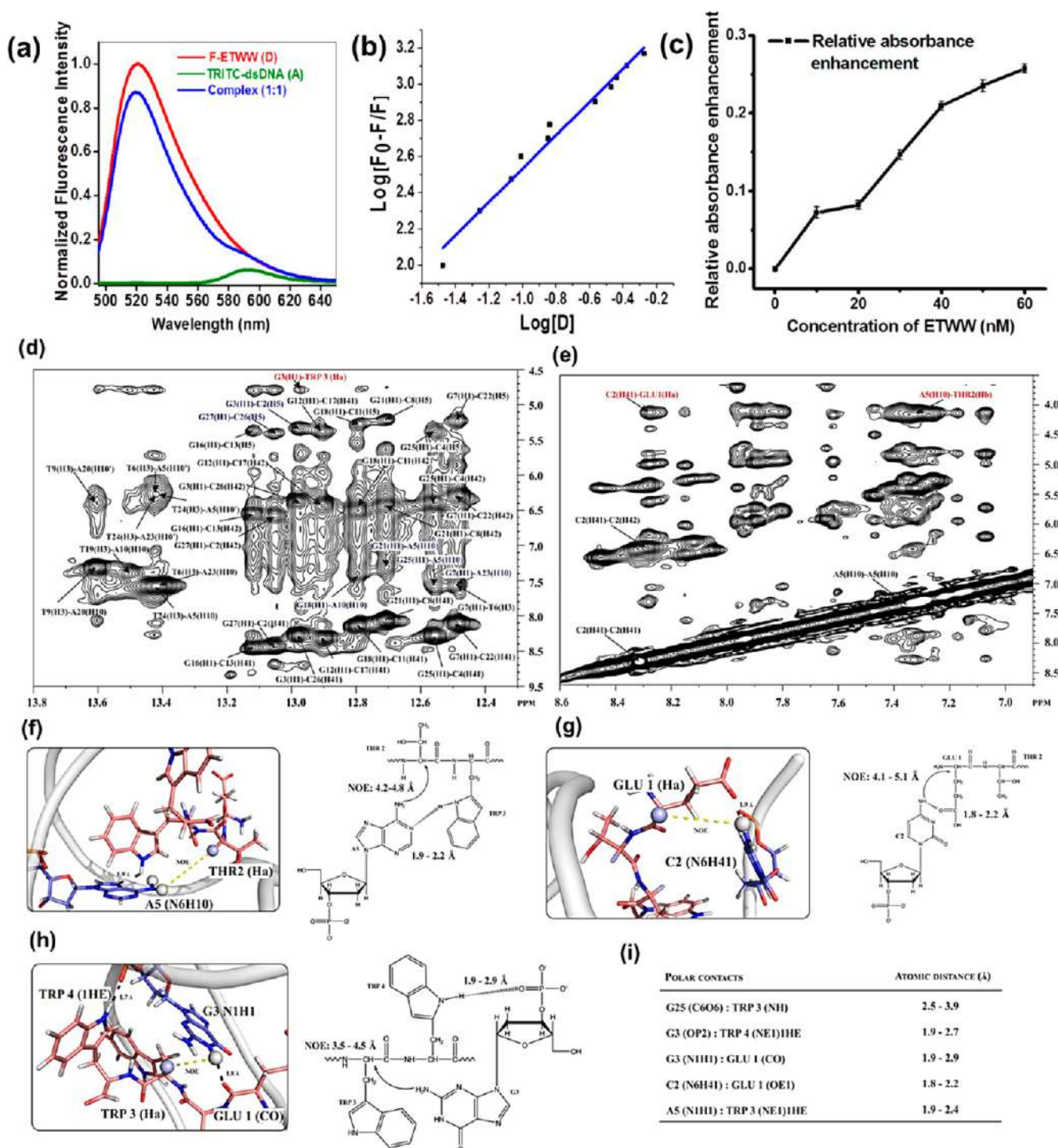
Figure 5. (a) Experiment reveals strong FRET between F-ETWW and TRITC-dsDNA upon incubation. (b) The fluorescence emission intensity of F-ETWW decreased with increasing concentration of dsDNA. Stern−Volmer plot of dsDNA titration with F-ETWW reveals a binding constant of $K_b = 2.84 \times 10^6$ M^{-1}, indicating strong interaction between peptide and dsDNA. (c) Relative absorbance enhancement of Methyl Green, confirming major groove binding of ETWW peptide at dsDNA. This gives a detailed account of ETWW−DNA interactions at the atomic level. Error bars represent standard deviation of the values. (d,e) Assignments of both exchangeable and non-exchangeable protons in the 2D NOESY spectra, revealing ETWW tetrapeptide−DNA contacts. (f−h) Polar contacts between specific amino acids and nucleotides generating NOE cross-peaks, represented in two and three dimensions. (i) List of polar contacts between dsDNA and ETWW tetrapeptide.

an affinity to bind on the outer surface of the receptor (Figure 3d and SI). In detail, the interactions are the >C═O group (−COOH) of glutamic acid with the −OH group of THR 195, and the −NH group (indole ring) of TRP 4 with the >C═O group of ALA 338. Also, the other tryptophan residue (TRP 3) of the tetrapeptide is in a hydrophobic interaction with PRO

219 and LEU 335 (receptor) (Figure S36). To validate the findings, we performed cellular uptake kinetics studies using 2 μM DOX or 5 μM F-ETWW in MCF7 cells via flow cytometry. Here we observed a time-dependent increase in cellular uptake of both molecules up to 2 h. After 2 h of incubation, the fluorescence intensity of DOX was found to be drastically

decreased, whereas F-ETWW's fluorescence gradually increased up to 6 h of experiment. This can be due to the fact that DOX is known to be a P-gp substrate and thus its cellular retention is affected, resulting in efflux and minimization of intracellular DOX fluorescence in cancer cells overexpressing P-gp receptor. Further, receptor-mediated endocytosis gradually enhances the ETWW localization in cells and due to its P-gp non-specificity, indicating efflux-independent retention of ETWW in cancer cells (Figures 3e and S37). These findings reveal that ETWW peptide is not a P-gp substrate and its cellular internalization could not be affected by this MDR efflux protein. Similar molecular docking of two non-successive tryptophan-containing tetrapeptides (WTWE and WETW) was performed with different receptors and efflux protein (Figure 3f–k and SI). Docking study indicates that both of them interact with the endothelin receptor with moderate binding energy (−7.4 and −7.7 kcal/mol) and also with mu opioid receptor with comparable binding energy (−8.1 and −8.1 kcal/mol). Moreover, docking of WTWE and WETW peptides with P-gp receptor confirmed that both peptides bind with MDR efflux protein with higher binding energy (−9.8 and −9.3 kcal/mol) compared to ETWW (−8.5 kcal/mol).

3.6. ETWW Retains Its DNA Binding Efficiency Even in the Metaphase Stage with the Condensed Chromatids.

Since ETWW has been found to bind to the major groove of DNA, we further investigated whether it retains its DNA-binding property during cell division. For this purpose, we performed an assay where we could monitor the interaction of peptide with chromatid DNA at the metaphase stage. To understand the chromatid binding potential of ETWW, we observed the cells in the metaphase stage having mitotic bipolar kinesin Eg5[41] with the condensed chromatids. When the cells were treated with 5 μM F-ETWW for 4 h, significant co-localization of our peptide was observed with the condensed chromatids stained with Hoechst 33258. It was clearly observed that, in the dividing mitotic cells, green ETWW peptide was co-localized with the DNA (blue) sandwiched between the red bipolar kinesin Eg5 (Figure 4 and SI). This result provides direct evidence that ETWW peptide retains its DNA-binding potential even in the dividing mitotic cells.

3.7. Monitoring Interaction of ETWW with dsDNA Using Molecular Docking, Förster Resonance Energy Transfer (FRET), and Titration Experiments.

Furthermore, to understand how ETWW specifically localizes into the nucleus and interacts with chromatin DNA, a blind docking experiment was performed between ETWW and dsDNA. This docking study unraveled the significant binding energy (BE = −7.9 kcal/mol) of ETWW into the major-groove-binding site of dsDNA (Figure S38). This result indicates that ETWW probably binds at the major groove of dsDNA with a strong affinity. Next, we performed a FRET study between F-ETWW (FRET donor, λ_{ex} = 485 nm) and rhodamine-labeled dsDNA (FRET acceptor, λ_{ex} = 540 nm) to understand how effectively ETWW binds with dsDNA. The Förster distance (R_0) between these two FRET pair dyes is 52.5 Å.[42] From FRET study and using the value of R_0 (52.5 Å), we calculated the distance between the donor−acceptor (R_{DA}) pair to be about 72 ± 2 Å, indicating a strong interaction between ETWW tetrapeptide and dsDNA. From Figure 5a, the emission maximum (λ_{max}) of the fluorescein-labeled peptide is found to be ~521 nm in phosphate buffer medium, while it becomes ~519 nm when bound to TRITC-labeled dsDNA. This indicates that TRITC-labeled DNA, under experimental conditions, binds strongly

with the tetrapeptide and exerts a more hydrophobic environment around F-ETWW (Figures 5a and S39). After performing FRET study, we were interested to determine the binding constant (K_b) between F-ETWW and dsDNA through titration experiment. The fluorescence emission intensity of F-ETWW decreased with increasing concentration of DNA. The K_b value was determined by calculating the decrease in F-ETWW peptide's fluorescence intensity using the Stern−Volmer equation and plotting against dsDNA concentration in μM (SI). It was found that the binding constant was K_b = 2.84 × 10⁶ M⁻¹, which indicates strong binding of ETWW with dsDNA (Figures 5b and S40).

3.8. ETWW Peptide Binding Location in dsDNA Confirmed by Groove-Binding Assays and 1D, 2D, and Relaxation NMR Experiments.

The above results clearly show that binding of ETWW with dsDNA is strong and possibly occurs at the major groove. Now, the concern is how to confirm that ETWW binds at the major groove but not the minor groove of the dsDNA. Therefore, the Methyl Green displacement assay was performed, as it has been well documented that Methyl Green is a major-groove-binding dye.[43] We used multiple oligonucleotide sequences having different distributions and abundances of AT and GC (Table T1). First, we co-incubated the Methyl Green and dsDNA sequences at room temperature for 10 min. We observed steady enhancement of absorbance of Methyl Green in the solution upon addition of increasing amounts of ETWW tetrapeptide. This result suggests that Methyl Green was displaced from the major groove of dsDNA and released into the solution, confirming that ETWW tetrapeptide has a strong affinity for the major groove. We calculated the IC₅₀ values for Methyl Green displacement by ETWW for each of the sequences, which do not significantly deviate from each other (Figure S41). Further, we estimated the binding parameters (affinity, number of occupied sites, and quenching constants) of ETWW for all the sequences, which suggest that ETWW binds the major groove of the DNA sequences irrespective of the sequence context (Figure S41). This observation was further confirmed by the DAPI displacement assay, since DAPI is known as a minor-groove-binding dye. In this experiment, we incubated DAPI with dsDNA for 10 min at room temperature. We observed insignificant changes in the fluorescence signal of DAPI upon addition of increasing amounts of ETWW tetrapeptide. This result clearly indicates that ETWW could not displace DAPI, which further proves that it has negligible affinity for the minor groove and high affinity for the major groove of dsDNA (Figures 5c and S42).

So far, we understand that ETWW can efficiently enter into the cell through an endocytosis process and localize into the nucleus through binding at the major groove of dsDNA. However, it is necessary to map out the binding interface of the peptide−dsDNA complex at the atomic level in order to gain insights into its mechanisms underpinning specific molecular recognition between ETWW and dsDNA's major groove. Initially, we recorded 1D ¹H NMR spectra of the free and ETWW tetrapeptide-bound dsDNA at each point of the titration and observed that the binding ratio between dsDNA and peptide was 3:10 (Figure S43). Further, we performed a 2D ¹H−¹H NOESY experiment for the ETWW−dsDNA complex to examine the effect of ETWW interactions on the structure and stability of the duplex (Figure 5d,e and SI). Recently, the solution NMR structure of the free dsDNA sequence has been resolved, which helped us to sequentially
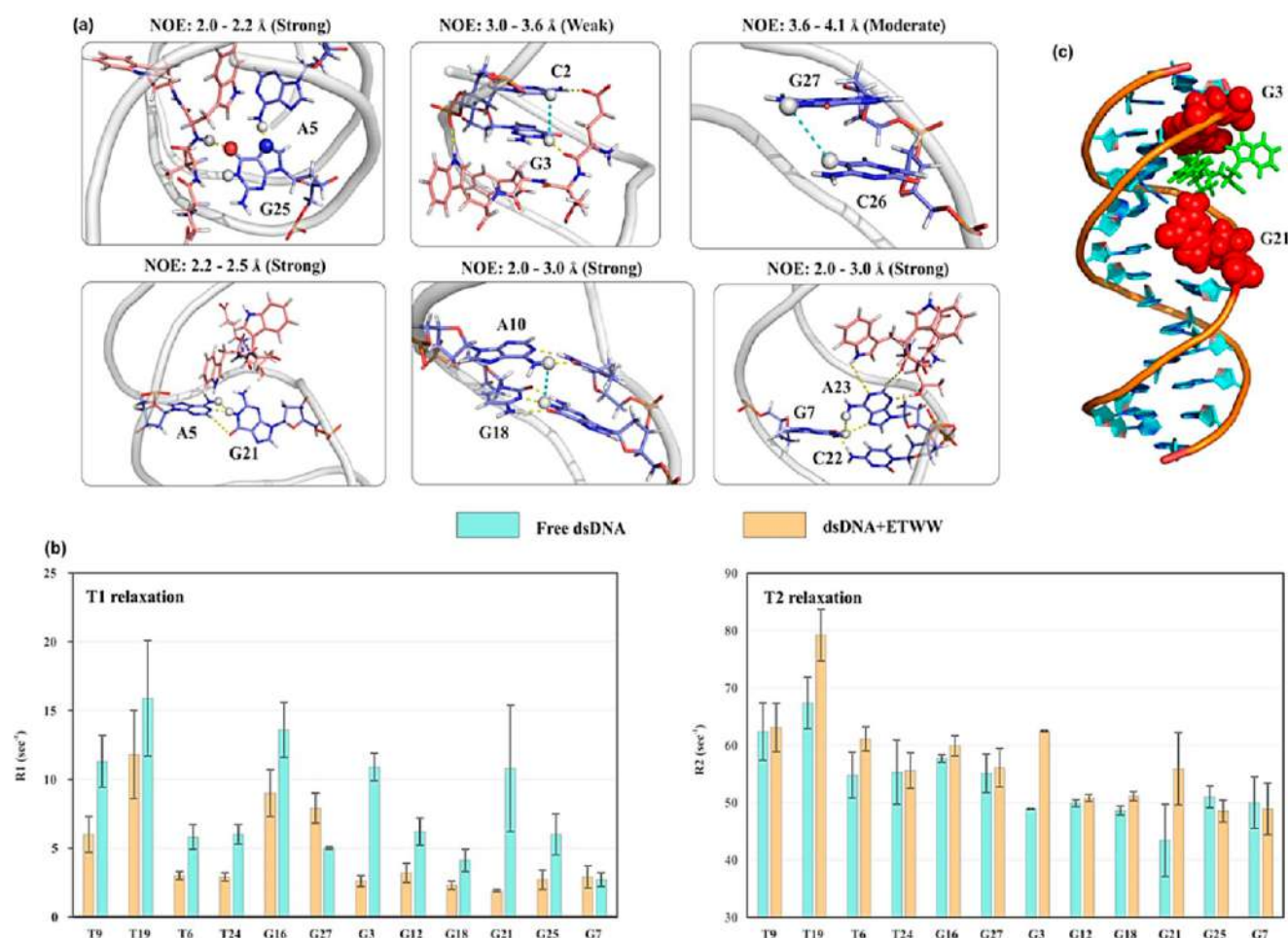
Figure 6. Dynamic characteristics of ETWW tetrapeptide−DNA interaction. (a) Rearrangement of Watson−Crick base-pairing and major groove geometry upon ETWW tetrapeptide interaction, which results in evolution of strong, moderate, and weak NOE cross-peaks that are not present in unbound dsDNA. (b) T1 and T2 relaxation profiles of ETWW tetrapeptide-bound and free dsDNA in terms of R1 (rate of T1 relaxation) and R2 (rate of T2 relaxation), respectively. (c) Modeled structure of the ETWW tetrapeptide-bound dsDNA showing G3 and G21, which are maximally affected due to interactions.

assign the exchangeable and non-exchangeable proton resonances of the duplex.[31] Superimposing the NOESY spectrum of the complex onto that of the unbound one reveals the evolution of new cross-peaks having strong NOEs, which is attributed to the intermolecular dipole−dipole interaction between the residues of ETWW and dsDNA in spatial proximity. These findings led us to identify specific DNA residues in the major groove involved in direct interaction with the peptide. Upon binding, one of the tryptophan residues (Trp4) in ETWW is oriented in a fashion to make strong electrostatic interactions with the phosphate backbone at the G3 residue, resulting in the evolution of a weak NOE signal between the imino proton of G3 and α-H of Trp 3. This interaction is strengthened by a stable hydrogen bond between C2 and the glutamic acid (Glu 1), which, in turn, evolves a strong NOE signal between the amino protons of C2 and α-H of Glu 1. Due to these polar contacts involving two tryptophan residues in trans positions and one glutamic acid like an arch in the wall of the major groove, G3 and C2 come in close proximity, resulting in a weak NOE signal between the C2 (H5) and G3 (N1H1) residues. Another stable contact is mapped out between A5 and threonine (Thr 2), which holds the peptide in a convex curvature at the major groove, resulting in a strong NOE signal

between the A5 amino protons and α-H of Thr 2 (Figure 5f−h and SI).

We also determined the polar contacts between dsDNA and ETWW (Figure 5i). These observations were further leveraged to inspect the geometry of the major groove in the duplex upon interaction for better illustration of the intra-residual connectivities in the complexed state compared to the unbound duplex. We observed intensified intra-residual NOEs at T9-, T6-, and T24-NH resonances in the bound DNA, which are involved in A:T base-pairs. These residues may not be directly involved in the peptide interaction, but they are stabilized and protected upon complex formation. This gives additional information regarding the changes in solvent accessibility of the interfacial DNA residues and provides further evidence of the DNA−peptide interface. Indeed, we observed strong NOE signals, providing direct evidence for stabilized G:C pairing in the complex, but we also found several weak signals, suggesting that the complex possesses significant conformational heterogeneity during the course of molecular recognition (Figure 6a and SI). Two strong NOE signals are observed between A5 (amino proton) and G21 (imino proton), and between A5 (amino proton) and G25 (imino proton), which probably appeared due to the perturbation in the normal Watson−Crick base-pairing of A5:T24, G21:C8, and G25:C4. Similarly, A23
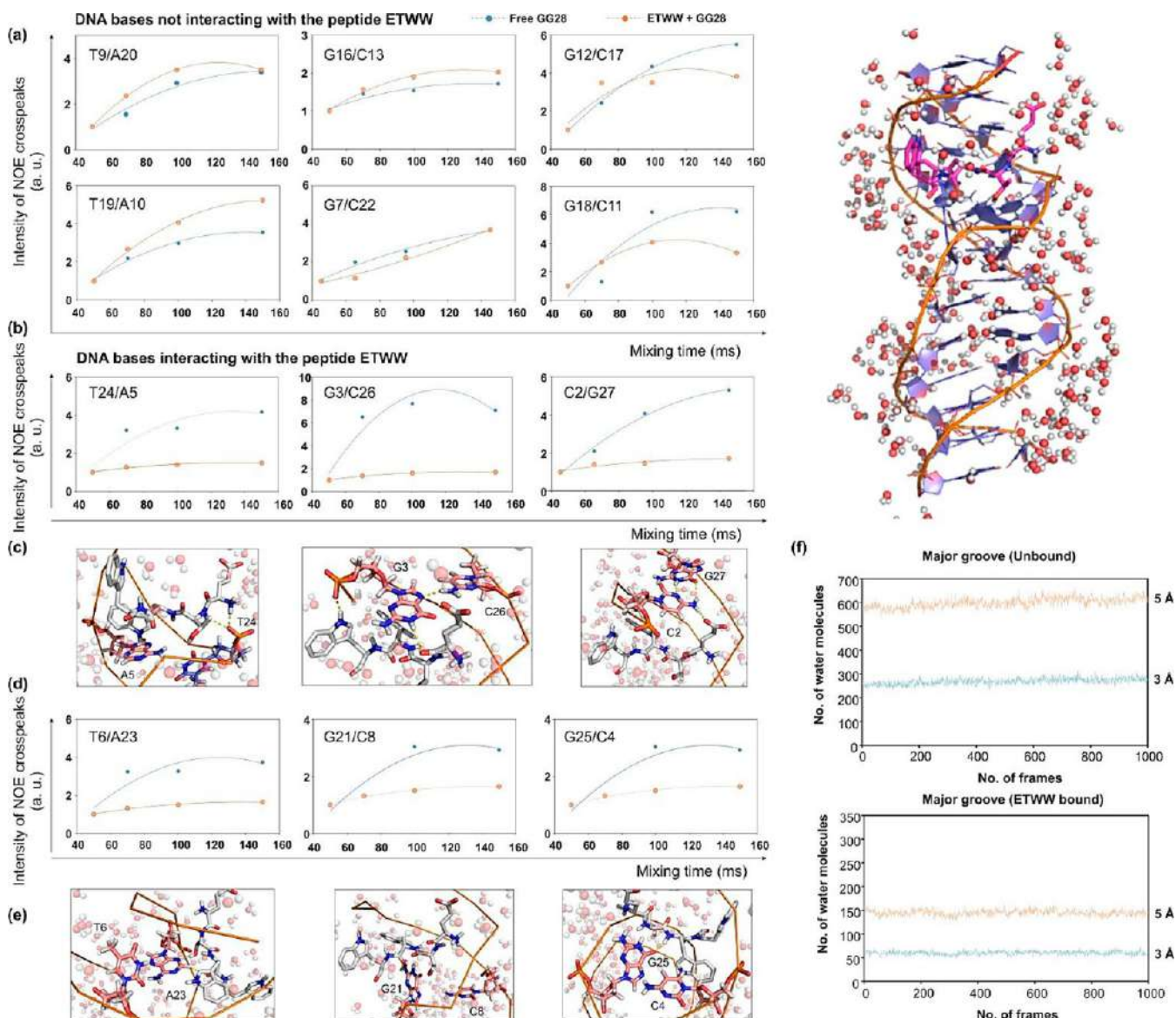
Figure 7. Role of water molecules in peptide–duplex interaction. (a) Intensity of the NOE cross-peaks plotted against mixing time for non-interacting DNA base-pairs which participate in interaction with ETWW. (b,d) Evolution of NOE intensity between exchangeable proton resonances and water for the base-pairs of interacting residues in the DNA major groove. (c,e) 3D picture of how peptide interaction removes water molecules from the binding cleft. (f) ETWW-DNA complex, shown with the first solvation layer. The water density is shown in 3 and 5 Å solvation layers under free and bound conditions.

interferes with G7:C22 base-pairing via a network of H-bonding interactions with Trp 3 and Glu 1 of ETWW. These result in the deformation of normal G:C pairing and appearance of a moderate NOE signal between the amino protons of A5 and imino proton of G7. Other strong NOE cross-peaks were observed between G18 (imino proton) and A10 (amino proton). Therefore, in ensemble terms, the unbound duplex consists of a conformational manifold, wherein the Watson–Crick base-pairing across the major-groove region has considerably greater conformational variation than the rest of the molecule upon ETWW interaction. Although the dynamic character of the major groove is restricted to some extent at the binding site, it does not achieve a level of rigidity. The bound state retains the conformational flexibility (to a lesser extent than free duplex), which leads us to represent the peptide-bound duplex as an ensemble of states rather than a discrete single structure. To further validate this conclusion, we performed induced-fit docking, which allows the major groove to alter its binding cleft such that the binding pose of the peptide comes in close proximity. We also minimized the complexes in implicit solvation and proposed three models of peptide–DNA complexes having the best IFD scores, which are in agreement with the prior structure calculations (Figure S44). The binding specificity of the peptide may be a function of the number of accessible conformations in the major groove that have the potential to facilitate low-energy contacts with ETWW.

These findings have significant consequences pertaining to the relationship between binding specificity and dynamic properties of the complex formation. Therefore, to determine the quantitative role of nucleic acid dynamics in the recognition process, it is necessary to analyze not only the average structure of the peptide-bound duplex but also the magnitude of conformational fluctuations during complexation. Since molec-

ular recognition of the peptide—dsDNA complex is associated with its surface properties, the major groove conformation of the double-helical DNA undergoes sufficient alteration in terms of flexibility, dynamics, and structure upon peptide interaction. To understand this, we performed a series of longitudinal (R1 = 1/T1) and transverse relaxation (R2 = 1/T2) experiments to investigate the dynamics of the ETWW tetrapeptide and dsDNA interaction on NMR time scales of fast to intermediate (μs—ms) (Figure 6b and SI). These dynamics are attributed to the DNA sequence under folding conditions, conformational properties, water exchange and accessibility, and binding of the peptide. The peptide—dsDNA association translates into shortened T2 relaxation time with concomitant escalation of the relaxation rates (R2), which envisages an overall increase in conformational heterogeneity due to a rise in correlation time, τ_c, and retardation of molecular tumbling rate upon ETWW titration. However, the relaxation rates in free states would also contain contributions from its local dynamics in the complex state in the case of faster exchange kinetics of ligand—DNA interaction. Shortening of the T2 relaxation time may also be attributed to fast exchange of protons between free and non-rotationally bound water molecules only. In the light of these results, it seems reasonable to conclude that changes in the degree of hydration of the dsDNA molecule occur before changes in stability of the hydrogen bonds between the complementary base-pairs in the DNA macromolecule. As opposed to T2 relaxation, the T1 relaxation time is increased upon complexation, resulting in repression in T1 relaxation rates. One plausible explanation is that the nucleobases, after binding to the ETWW, deflect from the stacked states, which results in a decrease of the rate of longitudinal relaxation of the imino protons. A stable complexation of peptide and duplex might have also influenced the intramolecular flexibility of the double-stranded DNA in which the localized motion of the flexible side chains slows down the dipolar relaxation by shortening the effective rotational correlation time, τ_c. Since rotational correlation time is inversely proportional to T1 relaxation time, shortening of τ_c results in a decrease in the T1 relaxation rate (R1). In the dynamics of both G3 and G21 imino protons, T1 and T2 relaxation profiles have pronounced effects upon complex formation, which indicates formation of stable contacts with the tetrapeptide in this region that attenuates the high-frequency motion across the major groove of the dsDNA (Figure 6c and SI). The above results clearly indicate that ETWW tetrapeptide binds at the major groove, and two successive tryptophan amino acids play significant roles in the overall stabilization of the peptide—dsDNA complex.

3.9. Mechanism of ETWW—Duplex Interaction in Solution.
Water molecules play an important role in solvating the macromolecules in peptide—duplex complexes and are located at the interface primarily to buffer the electrostatic repulsions between phosphate groups of DNA and the electronegative atoms on the protein. A small population of water molecules act as extended side chains to bridge the H-bond donor atoms in the peptide to the acceptor atoms in double-helical DNA. Earlier studies have proposed that water molecules mediate hydrogen-bonding networks that link side-chain and main-chain atoms of the peptides with the functional groups on the nucleobases and the anionic oxygen atoms of the phosphodiester backbone.[44] Sometimes, atoms of peptides involved in duplex interactions occupy positions normally occupied by water molecules in unbound conditions. To gain

further insight into the role of water molecules in the ETWW—duplex interaction, we performed a Watergate NOESY experiment under free and peptide-bound conditions, further substantiated by MD simulations in explicit solvent followed by water density calculation (Figure 7). Indeed, the cross-peak intensities between water and exchangeable imino protons of A:T and G:C pairs escalate upon increasing the mixing time. However, weaker cross-peaks are observed between water and the imino proton resonances, which exhibit stronger NOEs with peptide atoms. The DNA residues, G3, C2, and A5, which participate in polar contacts with Trp4, Glu1, and Thr2, show weaker NOEs between water and imino proton resonances. In contrast, the magnitude of water exchange does not alter for non-interacting base-pairs. MD simulations show that the stabilized network of non-covalent interactions between peptide and DNA reduces the solvent accessibility of the major groove compared to the free counterpart. This implies that the peptide, upon interaction with the major groove, deprives the water molecules from the binding cleft that serve to buffer electrostatic repulsions between electronegative atoms of the peptide and GG28.

3.10. Application of ETWW as Drug Delivery Vehicle.
We found that ETWW can efficiently enter into a cancer cell following an endocytosis mechanism and specifically localize into the nucleus and interact with chromatin DNA at the major groove. This result motivated us to explore whether ETWW can be useful as a cell-penetrating and nucleus-specific ligand for fabrication of an efficient drug delivery vehicle. For this purpose, in the work described in this Article, we have designed and developed a nano-liposome tagged with ETWW for successful and efficient delivery of nucleus-specific drugs.

3.11. Human Serum Stability of ETWW Performed by High-Performance Liquid Chromatography (HPLC).
Before fabrication of the ETWW-tagged nano-liposome-based drug delivery vehicle, we checked the stability of ETWW in human serum, which is important for the ligand of the drug delivery vehicle. ETWW was incubated with human serum as previously described up to 24 h and monitored using HPLC.[45−47] It was observed that 10% ETWW remained stable after 24 h incubation with human serum, indicating its good stability (Figure S45).

3.12. Penetration Ability of ETWW in Stem-Cell-Like, Tumor-Mimicking Multi-cellular 3D (Spheroid) Cell Culture.
Once the serum stability of ETWW peptide up to 24 h was confirmed, the penetration efficacy of F-ETWW inside tumor-mimicking multi-cellular 3D spheroid was investigated. Although anticancer drugs or drug formulations show significant anticancer effects in 2D animal model cell culture, they often fail to show potential effect against cancer stem cells and tumors. This is due to the poor ability of the therapeutic molecule to penetrate into the tumor. For this reason, we evaluated the penetration ability of ETWW in a tumor-mimicking, stem-cell-like multi-cellular 3D cell culture (spheroid) system. This assay reveals the effectiveness of drug or drug delivery systems in drug-resistant cancer, since this culture contains a high population of stem cells. Thus, a rational strategy would be to evaluate drugs or their formulations in the stem-cell-like 3D multi-cellular cell culture (spheroid) prior to evaluation in animal models. Accordingly, first 3D spheroids of B16F10 cells were prepared following our previously developed method.[48] In brief, B16F10 cells were cultured in DMEM-containing media and incubated in a humidified atmosphere with 5% CO_2 for a few days until the sizes of the spheroids
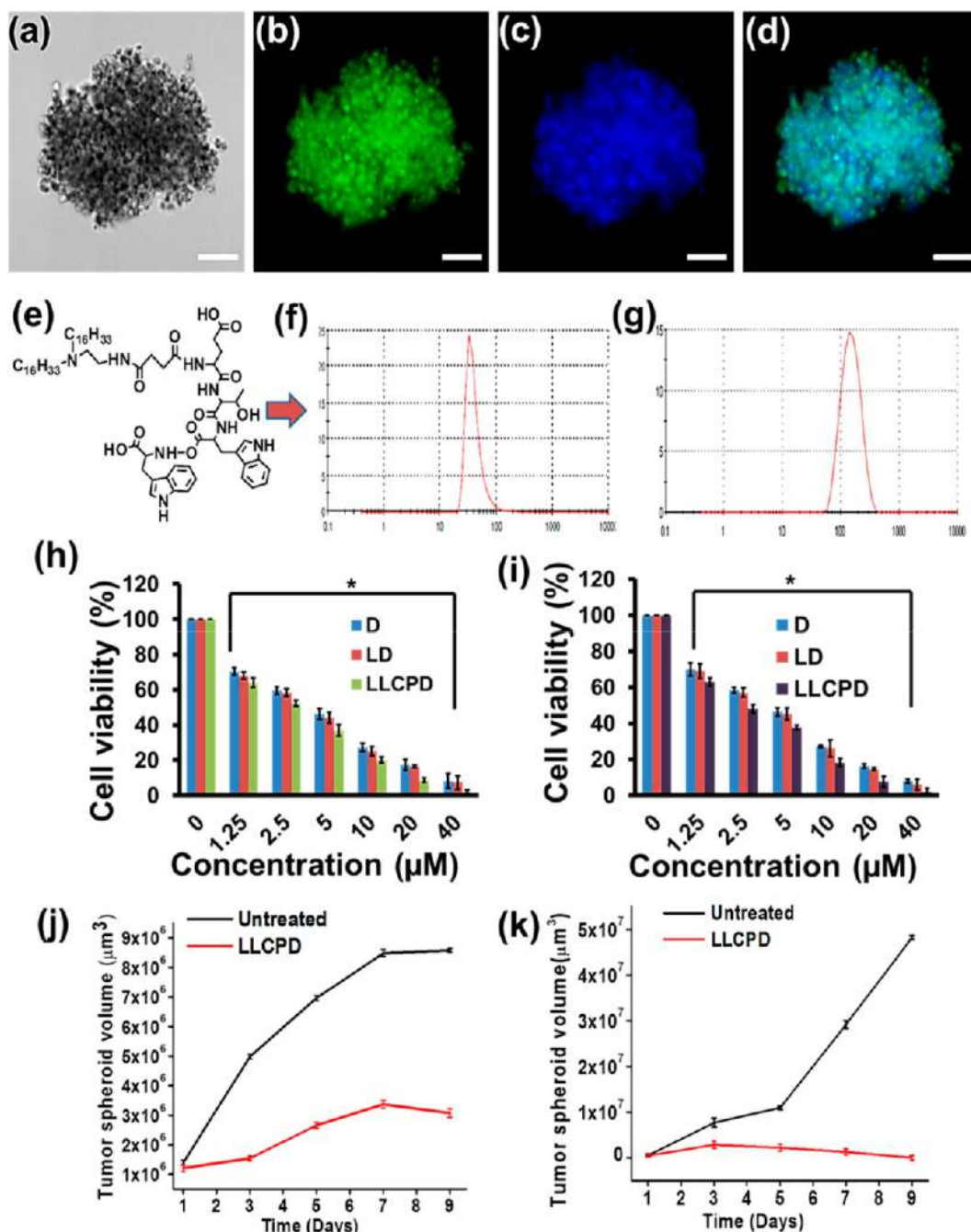
Figure 8. Penetration and dispersion of F-TP inside stem-cell-like multi-cellular (spheroids) cultures formed by B16F10 cells where nuclei are stained with Hoechst 33258. Images captured in (a) DIC mode, (b) at 488 nm, (c) at 405 nm, and (d) merged image. Images clearly indicate that F-TP penetrates through multiple layers of cells (stem cells) and specifically localizes at the nucleus. Scale bars correspond to 100 μm. (e) Structure of synthesized ETWW-lipopeptide (C16-ETWW). Size of liposome determined by DLS method indicating enhancement of sizes upon drug (DOX) loading, (f) normal liposome, and (g) LLCPD. Comparative cell viability assay of DOX (D), liposomal DOX (LD), and liposomal long-chain-attached ETWW peptide encapsulated with DOX (LLCPD) checked in (h) MCF7 and (i) B16F10 cells at various DOX concentrations (*$p <$ 0.0001, performing one-way ANOVA). Spheroid growth inhibition studies were performed after LLCPD treatment up to 9 days in (j) MCF7 and (k) B16F10 cells. Error bars represent standard error of the value.

reached up to 100 μm. We then checked the penetration and dispersion ability of F-ETWW inside spheroids of B16F10 cells. The nucleus of the cells was stained with Hoechst 33258 for 1 h. Spheroid co-localization images clearly indicate excellent co-localization of green fluorescence from F-ETWW with blue fluorescence from Hoechst 33258 (Figure 8a−d and SI). This result further proves that ETWW can successfully penetrate into the stem-cell-like 3D cell culture (spheroid), which clearly

indicates that it has strong ability to penetrate through multiple layers of cells, and thus it can play a crucial role in therapeutic delivery into the tumor.

3.13. Synthesis of Lipopeptide (C16-ETWW) for Fabrication of ETWW-Embedded Nano-liposome. We synthesized ETWW-lipopeptide (C16-ETWW) using SPPS method (SI), purified by HPLC and characterized by MALDI-TOF (Figures 8e and S46 and Scheme Sc2). After that, we
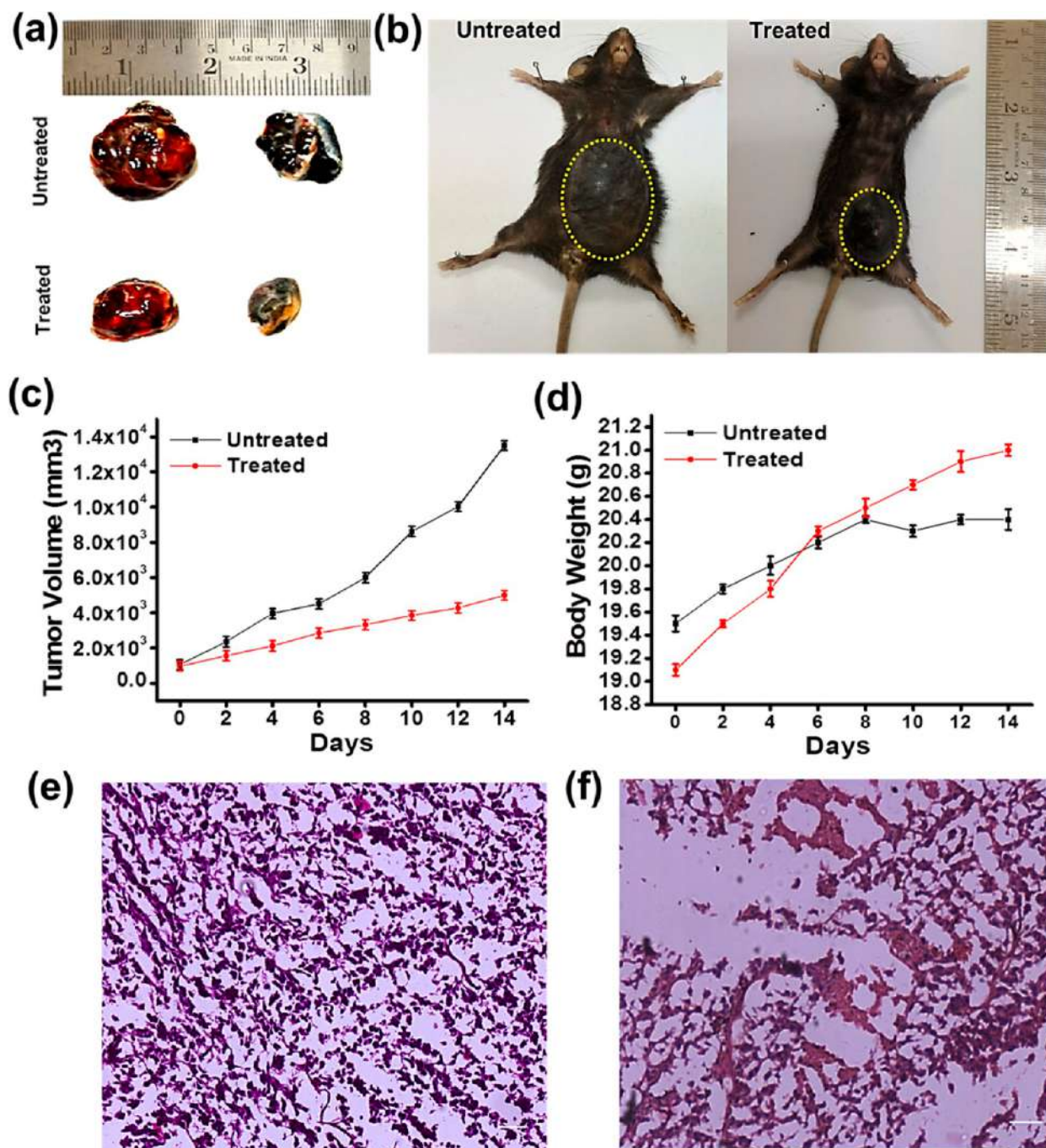
Figure 9. Efficacy of LLCPD in melanoma tumor. (a) Size of the tumors for both treated and untreated mice. (b) Representative mice images after treatment of LLCPD with respect to untreated control. (c) Graphical representation showing inhibition of tumor growth (tumor volume) upon LLCPD treatment compared to the untreated control. (d) Variation of mouse body weight upon treatment with LLCPD compared to the untreated groups. Comparative immunohistochemistry images of LLCPD-treated tumor (f) and untreated (e). Scale bar corresponds to 100 μm.

prepared ETWW-embedded liposome (LLCP) by hydration method using DOPC, cholesterol, and C16-ETWW as nucleus-specific drug delivery vehicles.[49]

3.14. Encapsulation of Anticancer Drug Doxorubicin (DOX) inside the ETWW-Embedded Liposome and Its Efficient Delivery into Human Breast Cancer Cells (MCF7). We prepared liposome embedded with long chain attached ETWW peptide containing doxorubicin (LLCPD) and liposome encapsulated with DOX in the absence of C16-ETWW (LD) following a previously described method (SI).[49,50] The amount of DOX entrapped inside the liposomes

was determined using absorbance measurement of liposome at 480 nm by UV spectrophotometer.[51] Further, the sizes of both LD and LLCPD were determined by cryo-EM and DLS, respectively. DLS study revealed LD and LLCPD to be 40 and 142 nm, respectively, indicating encapsulation of DOX (Figures 8f,g and S47). After complete characterization of drug encapsulation inside the liposomes and their sizes, we checked their drug delivery efficiency into MCF7 cells. We know that DOX is the classical DNA topoisomerase inhibitor and specifically binds at the nucleus. First, we used fluorescence microscopy imaging for monitoring the drug delivery efficiency.

Fluorescence microscopy revealed that a significant amount of DOX was localized in the nucleus in the case of LLCPD compared to LD and DOX alone, respectively, in MCF7 cells (Figure S48). This result clearly suggests that ETWW significantly enhances the DOX delivery efficiency in the nucleus. Next, we performed cell viability study of LLCPD at various concentrations of encapsulated DOX along with required control liposomes. The cell viability study reveals that the toxicity of LLCPD is significantly high (IC$_{50}$ = 2.7 ± 0.2 μM) compared to that of LD and DOX alone (IC$_{50}$ = 3.6 ± 0.1 μM) in MCF7 cells (Figure 8h and SI).

3.15. Design of Animal Model To Validate Effectiveness of LLCPD. We further validated whether our delivery system is effective in an animal model. To do so, we checked the effectiveness of LLCPD in a mice melanoma model as proof of concept. In brief, this model was generated through subcutaneous injection of mice melanoma cells (B16F10) into live mice (~2 × 10^6 cells/mouse).[48] For this purpose, we first evaluated the effect of LLCPD on B16F10 cells. Interestingly, we observed that the IC$_{50}$ value of LLCPD is significantly low (IC$_{50}$ = 2.4 ± 0.1 μM) compared to that of DOX alone (IC$_{50}$ = 3.5 ± 0.3 μM) in B16F10 (Figure 8i and SI).

3.16. Effect of LLCPD in Stem-Cell-Like, Tumor-Mimicking Multi-cellular 3D (Spheroid) Cell Culture System. Before evaluation of LLCPD in a mice melanoma model, we tested LLCPD in the stem-cell-like, tumor-mimicking multi-cellular 3D (spheroid) cell culture system of both B16F10 and MCF7. Accordingly, 3D spheroids of B16F10 and MCF7 were prepared as described above.[47] Spheroids were distributed into two sets, one for treatment with LLCPD and an untreated control. LLCPD and untreated spheroid volumes were imaged, and their sizes were monitored under a microscope up to 9 days from the day of treatment. We observed significant inhibition of growth for LLCPD-treated spheroids compared to the untreated control in both B16F10 and MCF7 spheroids (Figures 8j,k, S49, and S50). All these *in vitro* experiments clearly showed that LLCP acts as an excellent drug delivery vehicle, where ETWW tetrapeptide plays a significant role.

3.17. Efficacy of LLCPD in Mice Melanoma Model. We next evaluated LLCPD in the *in vivo* mice melanoma model. In brief, we chose 7-week-old C57BL/6J female mice having average body weight of 15−17 g. Animals were placed in a pathogen-free laboratory environment throughout the experiments, maintaining standard guidelines of our animal house. Melanoma tumors were developed in the mice through one-time subcutaneous injection of mice melanoma B16F10 cells (~2 × 10^6 cells/animal). Development of tumors was monitored daily using slide callipers, and tumor volume was calculated by the formula $V = 0.5 \times$ length × width^2. Mice were randomly divided into the two groups after the average tumor volume reached nearly 1000 mm^3 (5 mice/group). First, group 1 and group 2 were divided as treated and untreated, respectively. Each member of group 1 was treated with LLCPD ([DOX] = 5 mg/kg) on the first and eighth days, and group 2 mice remained untreated. We then monitored tumor growth inhibition, tumor volume, and mice body weight up to 14 days. Each day tumor volume and body weight were measured. After 14 days, mice were sacrificed and tumors were collected followed by volume measurement (SI). It was observed that tumor sizes remained almost constant for treated mice, whereas for the control group tumor sizes increased

extensively (Figure 9a−c and SI). We observed that the body weight of mice increased steadily in the case of the treated group compared to the untreated (control) group (Figure 9d and SI). Tumors were sectioned with a thickness of 4 μm by Leica rotary microtome. Slices were stained with H&E for histological study (Figure 9e,f and SI). Interestingly, immunohistochemistry data reveal high amounts of damaged tumor cells, tumor muscles, and blood vessels in the case of the treated tumor, which indicates the effectiveness of ETWW-lipopeptide-embedded liposome containing doxorubicin in treating melanoma.

3.18. Effect of ETWW in Adrenal Pheochromocytoma (PC12) Cell-Line-Derived Neuron Cell Culture. It has been demonstrated before that CPPs often cause additive amyloidogenic effects once they enter into the brain.[29] Now the question is whether ETWW has any toxic effect in the brain or neurons, as the above results successfully demonstrated that ETWW can be utilized as an excellent CPP as well as nuclear-localizing peptide.

As a preliminary experiment we checked whether ETWW has an effect on cell viability and morphology of PC12-derived neurons. PC12 cell-line-derived neurons were treated with ETWW at various concentrations ranging from 1.56 to 200 μM. The cells were found to be viable at even higher concentrations, revealing that our peptide has no toxic effect on neuronal health. Additionally, PC12-derived neurons treated with 50 μM ETWW were observed under a microscope in DIC mode, and they were found to maintain their healthy morphology as compared to the untreated sample (Figure S51). These results confirm that ETWW is non-cytotoxic against PC12-derived neuronal cells and the cells retain their healthy morphology.

4. DISCUSSION

Our results demonstrate an anionic cell-penetrating tetrapeptide truncated from Pep1 containing successive tryptophan amino acids, which carries one negative charge due to the presence of one glutamic acid (E). Although there are a few anionic CPPs known,[52,53] to the best of our knowledge anionic tetramer CPP has not been reported before. Further, we found that successive trp-trp sequence in ETWW and other tetrapeptides plays a significant role in cell penetration and nuclear localization. In contrast, tetrapeptides having spacer amino acids between trp-trp residues failed to localize at the cell nucleus and showed significant reduction in cell penetration. This interesting observation reveals the influence of tryptophans in a short tetrapeptide when they are together. We demonstrated initially in a qualitative manner how six tetrapeptides containing trp-trp dipeptide efficiently enter into cancer cells, specifically localizing into the nucleus even in the presence of minor-groove-binding dye Hoechst 33258. This result provided the first clue that tetrapeptides containing the trp-trp sequence localize at the nucleus through binding at nuclear DNA. Subsequently, we found that tetrapeptides containing trp-trp dipeptide specifically interact with dsDNA on a 2D micropatterned chip, while tetrapeptides containing non-successive tryptophan are unable to bind with dsDNA on a 2D micropatterned chip. This result provides further insight that trp-trp in tetrapeptides plays a crucial role in their interactions with DNA. We found that, among all the tetrapeptides, ETWW exhibits the highest potential in cell penetration and nuclear localization. Moreover, we found that ETWW tetrapeptide successfully enters into the cancer cell through an endocytosis mechanism, where two tryptophan

amino acids play an important role. Using molecular docking experiments, we found that ETWW tetrapeptide strongly interacts with endothelin and mu opioid receptor proteins at the cell surface. This result supports our view that the cellular entry of ETWW occurs through an endocytosis mechanism.

It is important to note that cellular availability of the molecule is not only proportional to its membrane receptor but also inversely related to multi-drug resistance (MDR) protein or P-glycoprotein (P-gp). Evaluation of the interaction between ETWW and P-gp receptor is crucial to understand the potential of ETWW as a CPP. Results from the "SwissADME" method revealed non-specificity of ETWW with P-gp and various CYPs, which motivated us to pursue a structure-based understanding of the possible interactions. Thus, molecular docking was performed between ETWW and the well-characterized (via crystallography) structure of P-gp receptor. The result showed that ETWW peptide did not interact with any reported binding sites (i.e., M, R, and H sites); rather, it has an affinity to interact at the outer surface of the P-gp receptor. These results indicate that ETWW peptide is not a P-gp substrate and its cellular internalization could not be affected by this MDR efflux protein. Next, using various experimental techniques, we learned that ETWW tetrapeptide binds strongly with dsDNA at the major-groove-binding site. Remarkably, we found that ETWW can retain its binding even in dividing cells, as we explored the binding of ETWW with chromatid DNA at the metaphase stage when immunostained with anti-Eg5 antibody. Further, we performed NMR experiments to understand at an atomic level how ETWW interacts with the major groove of dsDNA. NMR study revealed that this tetrapeptide interacts with the DNA major groove with G3 and G21. 2D NOESY spectra confirmed the higher stability of the duplex along the major groove through imino–amino contacts. Overall, NMR results revealed that ETWW binds with dsDNA in an arch-shaped conformation through electrostatic, H-bonding, and stacking interactions, where two tryptophan amino acids play a crucial role. Tryptophans in adjacent positions form a network of non-covalent interactions which remove the water molecules from the binding groove and stabilize the complex, giving an intuitive picture of solvent interactions of the peptide–duplex complex similar to that of the cellular microenvironment.

These results motivated us to explore whether ETWW can be used as a ligand because of its excellent cell penetration and nuclear localization ability. Interestingly, we found that ETWW can easily penetrate through multi-cellular 3D cell culture (spheroid) and localize at the cell nucleus, which in fact is highly populated with stem cells. This result clearly demonstrates that ETWW is able to not only penetrate through multiple cell layers but also enter into the stem cells. Further, results showed that ETWW-embedded liposome serves as an excellent drug delivery vehicle. We showed that this carrier can specifically deliver doxorubicin to the nucleus of a cancer cell with high efficiency. Similarly, when ETWW was present as ligand on the liposome, we observed excellent penetration ability of the delivery vehicle not only into the 2D cancer cell but also into the multi-cellular 3D cell culture (spheroid). It efficiently delivered doxorubicin drug specifically into the nucleus of the cells inside the spheroid, significantly inhibiting the growth of tumor-mimicking 3D spheroids of both MCF7 and B16F10 cells compared to the control liposome (absence of ETWW ligand). Further, it has been emphasized that these multi-cellular spheroids are basically rich in stem cells, and we are contented to see that our delivery vehicle has

penetration capability into the stem cells of both MCF7 and B16F10.

Next, we confirmed that this liposome system containing doxorubicin significantly reduces tumor growth in a mice melanoma model. Finally, we evaluated the effect of ETWW in PC12-derived neurons culture, since CPPs may cause additive amyloidogenic effects in the brain. We found that ETWW is non-cytotoxic against PC12-derived neurons and does not affect their morphology.

5. CONCLUSION

In summary, we discovered a new short cell-penetrating peptide. We convincingly determined that the trp-trp dipeptide-containing tetrapeptide can be useful as a good, non-cytotoxic anionic CPP that specifically localizes in the cell nucleus by interacting with the major groove of DNA. Moreover, we found that it is not a P-gp substrate and does not cause additive amyloidogenic effects in PC12-derived neurons. Finally, its potential as a CPP was validated in multi-cellular 3D cell culture (spheroid) and in an *in vivo* mice model. This study provides major fundamental insights about the positional importance of tryptophan and opens new directions toward the development of next-generation CPPs and major-groove binders. Overall, these findings suggest new conceptual platforms for designing aggressive CPPs, which can be extremely useful for specifically delivering major-groove-binding anticancer drugs and may serve as excellents template for designing major-groove-specific anticancer drugs.

■ ASSOCIATED CONTENT

ⓈSupporting Information
The Supporting Information is available free of charge on the ACS Publications website at DOI: 10.1021/jacs.7b10254.

Experimental details regarding peptide and lipopeptide synthesis, cell culture, microscopic, docking, flow cytometry assays, FRET study, major and minor groove binding study, 1D and 2D NMR, and *in vitro* and *in vivo* studies; Schemes Sc1 and Sc2, Table T1, and Figures S1–S51 (PDF)

■ AUTHOR INFORMATION

Corresponding Author
*sghosh@iicb.res.in

ORCID ⓘ
Debmalya Bhunia: 0000-0001-8649-0466
Prasenjit Mondal: 0000-0003-0767-449X
Surajit Ghosh: 0000-0002-8203-8613

Author Contributions
#D.B. and P.M. contributed equally as first authors.

Author Contributions
⊥A.S. and P.S. contributed equally as third authors.

Notes
The authors declare no competing financial interest.

■ REFERENCES

(1) Frankel, A. D.; Pabo, C. O. *Cell* **1988**, *55*, 1189−1193.

(2) Green, M.; Loewenstein, P. M. *Cell* **1988**, *55*, 1179−1188.

(3) Joliot, A.; Pernelle, C.; Deagostini-Bazin, H.; Prochiantz, A. *Proc. Natl. Acad. Sci. U. S. A.* **1991**, *88*, 1864−1868.

(4) Derossi, D.; Joliot, A. H.; Chassaing, G.; Prochiantz, A. *J. Biol. Chem.* **1994**, *269*, 10444−10450.

(5) Derossi, D.; Calvet, S.; Trembleau, A.; Brunissen, A.; Chassaing, G.; Prochiantz, A. *J. Biol. Chem.* **1996**, *271*, 18188−18193.

(6) Vives, E.; Brodin, P.; Lebleu, B. *J. Biol. Chem.* **1997**, *272*, 16010−16017.

(7) Mitchell, D. J.; Kim, D. T.; Steinman, L.; Fathman, C. G.; Rothbard, J. B. *J. Pept. Res.* **2000**, *56*, 318−325.

(8) Futaki, S. *Int. J. Pharm.* **2002**, *245*, 1−7.

(9) Wright, L. R.; Rothbard, J. B.; Wender, P. A. *Curr. Protein Pept. Sci.* **2003**, *4*, 105−124.

(10) Futaki, S.; Suzuki, T.; Ohashi, W.; Yagami, T.; Tanaka, S.; Ueda, K.; Sugiura, Y. *J. Biol. Chem.* **2001**, *276*, 5836−5840.

(11) Vives, E.; Granier, C.; Prevot, P.; Lebleu, B. *Lett. Pept. Sci.* **1997**, *4*, 429−436.

(12) Rothbard, J. B.; Kreider, E.; VanDeusen, C. L.; Wright, L.; Wylie, B. L.; Wender, P. A. *J. Med. Chem.* **2002**, *45*, 3612−3618.

(13) Delaroche, D.; Aussedat, B.; Aubry, S.; Chassaing, G.; Burlina, F.; Clodic, G.; Bolbach, G.; Lavielle, S.; Sagan, S. *Anal. Chem.* **2007**, *79*, 1932−1938.

(14) Salonen, L. M.; Ellermann, M.; Diederich, F. *Angew. Chem., Int. Ed.* **2011**, *50*, 4808−4842.

(15) Walrant, A.; Correia, I.; Jiao, C.; Lequin, O.; Bent, E. H.; Goasdoué, N.; Lacombe, C.; Chassaing, G.; Sagan, S.; Alves, I. D. *Biochim. Biophys. Acta, Biomembr.* **2011**, *1808*, 382−393.

(16) Fischer, P. M.; Zhelev, N. Z.; Wang, S.; Melville, J. E.; Fahraeus, R.; Lane, D. P. *J. Pept. Res.* **2000**, *55*, 163−172.

(17) Killian, J. A.; von Heijne, G. *Trends Biochem. Sci.* **2000**, *25*, 429−434.

(18) White, S. H.; Wimley, W. C. *Annu. Rev. Biophys. Biomol. Struct.* **1999**, *28*, 319−365.

(19) Killian, J. A.; Burger, K. N.; de Kruijff, B. *Biochim. Biophys. Acta, Biomembr.* **1987**, *897*, 269−284.

(20) Chan, D. I.; Prenner, E. J.; Vogel, H. J. *Biochim. Biophys. Acta, Biomembr.* **2006**, *1758*, 1184−1202.

(21) Rydberg, H. A.; Matson, M.; Amand, H. L.; Esbjorner, E. K.; Norden, B. *Biochemistry* **2012**, *51*, 5531−5539.

(22) Morris, M. C.; Depollier, J.; Mery, J.; Heitz, F.; Divita, G. A. *Nat. Biotechnol.* **2001**, *19*, 1173−1176.

(23) Deshayes, S.; Morris, M. C.; Divita, G.; Heitz, F. *J. Pept. Sci.* **2006**, *12*, 758−765.

(24) Deshayes, S.; Morris, M. C.; Divita, G.; Heitz, F. *Biochim. Biophys. Acta, Biomembr.* **2006**, *1758*, 328−335.

(25) Kondo, E.; Seto, M.; Yoshikawa, K.; Yoshino, T. *Mol. Cancer Ther.* **2004**, *3*, 1623−1630.

(26) Munoz-Morris, M. A.; Heitz, F.; Divita, G.; Morris, M. C. *Biochem. Biophys. Res. Commun.* **2007**, *355*, 877−882.

(27) Deshayes, S.; Plenat, T.; Charnet, P.; Divita, G.; Molle, G.; Heitz, F. *Biochim. Biophys. Acta, Biomembr.* **2006**, *1758*, 1846−1851.

(28) Henriques, S. T.; Quintas, A.; Bagatolli, L. A.; Homble, F.; Castanho, M. A. *Mol. Membr. Biol.* **2007**, *24*, 282−293.

(29) Giunta, B.; Ehrhart, J.; Obregon, D. F.; Lam, L.; Le, L.; Jin, J.; Fernandez, F.; Tan, J.; Shytle, R. D. *Mol. Brain* **2011**, *4*, 23.

(30) Pjura, P. E.; Grzeskowiak, K.; Dickerson, R. E. *J. Mol. Biol.* **1987**, *197*, 257−271.

(31) Ghosh, A.; Kar, R. K.; Jana, J.; Saha, A.; Jana, B.; Krishnamoorthy, J.; Kumar, D.; Ghosh, S.; Chatterjee, S.; Bhunia, A. *ChemMedChem* **2014**, *9*, 2052−2058.

(32) Biswas, A.; Saha, A.; Jana, B.; Kurkute, P.; Mondal, G.; Ghosh, S. *ChemBioChem* **2013**, *14*, 689−694.

(33) Zoete, V.; Daina, A.; Bovigny, C.; Michielin, O. J. *J. Chem. Inf. Model.* **2016**, *56*, 1399−1404.

(34) Gfeller, D.; Michielin, O.; Zoete, V. *Bioinformatics* **2013**, *29*, 3073−3079.

(35) Shihoya, W.; Nishizawa, T.; Okuta, A.; Tani, K.; Dohmae, N.; Fujiyoshi, Y.; Nureki, O.; Doi, T. *Nature* **2016**, *537*, 363−368.

(36) Cui, X.; Yeliseev, A.; Liu, R. *Eur. J. Pharmacol.* **2013**, *702*, 309−315.

(37) Sharom, F. J. *J. Membr. Biol.* **1997**, *160*, 161−175.

(38) Oude Elferink, R. P. J.; Zadina, J. *Peptides* **2001**, *22*, 2015−2020.

(39) Aller, S. G.; Yu, J.; Ward, A.; Weng, Y.; Chittaboina, S.; Zhuo, R.; Harrell, P. M.; Trinh, Y. T.; Zhang, Q.; Urbatsch, I. L.; Chang, G. *Science* **2009**, *323*, 1718−1722.

(40) Ferreira, R. J.; Ferreira, M. J.; dos Santos, D. J. *J. Chem. Inf. Model.* **2013**, *53*, 1747−1760.

(41) Banerjee, M.; Singh, P.; Panda, D. *FEBS J.* **2010**, *277*, 3437−3448.

(42) Hiller, D. A.; Fogg, J. M.; Martin, A. M.; Beechem, J. M.; Reich, N. O.; Perona, J. J. *Biochemistry* **2003**, *42*, 14375−14385.

(43) Kim, S. K.; Nordén, B. *FEBS Lett.* **1993**, *315*, 61−64.

(44) Jayaram, B.; Jain, T. *Annu. Rev. Biophys. Biomol. Struct.* **2004**, *33*, 343.

(45) Prades, R.; Oller-Salvia, B. S.; Schwarzmaier, M.; Selva, J.; Moros, M.; Balbi, M.; Grazu, V.; de La Fuente, J. M.; Egea, G.; Plesnila, N.; Teixido, M.; Giralt, E. *Angew. Chem., Int. Ed.* **2015**, *54*, 3967−3972.

(46) Jana, B.; Mondal, P.; Saha, A.; Adak, A.; Das, G.; Mohapatra, S.; Kurkute, P.; Ghosh, S. *Langmuir* **2017**, DOI: 10.1021/acs.langmuir.7b01326.

(47) Rajasekhar, K.; Madhu, C.; Govindaraju, T. *ACS Chem. Neurosci.* **2016**, *7*, 1300−1310.

(48) Bhunia, D.; Mohapatra, S.; Kurkute, P.; Ghosh, S.; Jana, B.; Mondal, P.; Saha, A.; Das, G.; Ghosh, S. *Chem. Commun.* **2016**, *52*, 12657−12660.

(49) Saha, A.; Mohapatra, S.; Das, G.; Jana, B.; Ghosh, S.; Bhunia, D.; Ghosh, S. *ACS Appl. Mater. Interfaces* **2017**, *9*, 176−188.

(50) Bhunia, D.; Saha, A.; Adak, A.; Das, G.; Ghosh, S. *RSC Adv.* **2016**, *6*, 113487−113491.

(51) de Lange, J. H.; Schipper, N. W.; Schuurhuis, G. J.; ten Kate, T. K.; Van Heijningen, T. H.; Pinedo, H. M.; Lankelma, J.; Baak, J. P. *Cytometry* **1992**, *13*, 571−576.

(52) Martín, I.; Teixidó, M.; Giralt, E. *ChemBioChem* **2011**, *12*, 896−903.

(53) Yamada, T.; Signorelli, S.; Cannistraro, S.; Beattie, C. W.; Bizzarri, A. R. *Mol. Pharmaceutics* **2015**, *12*, 140−149.

Apoferritin Nanocage Delivers Combination of Microtubule and Nucleus Targeting Anticancer Drugs

Subhajit Ghosh,[†] Saswat Mohapatra,[‡] Anisha Thomas,[§] Debmalya Bhunia,[†] Abhijit Saha,[†] Gaurav Das,[‡] Batakrishna Jana,[†] and Surajit Ghosh*,[†,‡]

[†]Organic and Medicinal Chemistry Division, CSIR—Indian Institute of Chemical Biology, 4 Raja S. C. Mullick Road, Jadavpur, Kolkata 700032, West Bengal, India

[‡]Academy of Scientific and Innovative Research (AcSIR), CSIR—Indian Institute of Chemical Biology Campus, 4 Raja S. C. Mullick Road, Kolkata 700032, India

[§]Department of Chemistry, Indian Institute of Technology Kanpur, Kanpur 208016, India

S *Supporting Information*

ABSTRACT: An ideal nano drug delivery agent must be potent enough to carry high dose of therapeutics and competent enough in targeting specific cell of interest, having adequate optimized physiochemical properties and biocompatibility. Carrying differentially polar therapeutics simultaneously will make them superior in their class. However, it is of enormous challenge to the researchers to find such a unique nanocarrier and to engineer all of the above-mentioned features into it. In this manuscript, we have shown for the first time that apoferritin (Apf) can carry and deliver high dose of doxorubicin (Dox), docetaxel (Doc), and combination of both Dox and Doc specifically into the cancer cell and enhances killing compared to free drug without any functionalization or property modulation. In addition, we have shown that Apf alone is noncytotoxic in nature and interacts with intracellular tubulin/microtubule. Drug loaded Apf specifically bound and consequently internalized into the human breast cancer cell line (MCF7) and human cervical cancer cell line (HeLa) through receptor mediated endocytosis process and releases either single or combination of drugs in the endosome. We have also checked the binding efficacy of both drugs using molecular docking. Further, using fluorescence microscopy, we have shown that Apf can deliver combination of drugs inside cancer cells and the drugs exerts their effect thereof. Finally, we have studied the efficacy of Apf complexes with individual drugs and in combination compared to free drugs in a tumor mimicking 3D multicellular spheroid model of HeLa cell.

KEYWORDS: apoferritin, drug delivery, combination therapy, cancer cell, tubulin/microtubule, spheroid
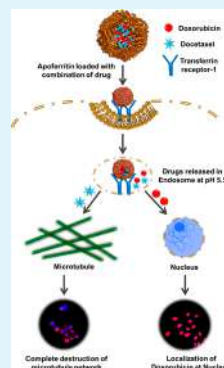
■ INTRODUCTION

Single-drug therapies for the treatment of cancers are ineffective over a long period of time.[1−4] Therefore, development of more potential combination therapies and understanding their detailed mechanism of actions are extremely important in the present situation. Recently, various combinations of drugs have been developed for treating various cancers targeting various intracellular components.[5−8] A few examples are (i) combination of doxorubicin and docetaxel for the treatment of the patients suffering from breast and prostate cancer,[9−12] (ii) combination of paclitaxel (PTX) and 5-fluoroucacil (5-FU) for patients suffering from gastric, breast, pancreatic, and other types of cancer,[13−15] (iii) combination of antifolate methotrexate, vincristine, 6-mercaptoturine, and prednisone for childhood acute lymphoblastic leukemia,[16] (iv) combination of vincristine, prednisone, nitrogen mustard, and procarbazine for testicular cancer, epithelial malignancies, colorectal, breast, and many others.[17] These drugs follow different mechanisms to kill tumor cells, and recent advances in our knowledge of cancer genomics and mechanisms of action of several drugs have paved the way for a better design of combination therapy for effective treatment of cancers. Although some combination drugs

show potent activity, major problems associated with these drugs, like bioavailability (poor solubility) and whole body toxicity, make them poor candidates for cancer therapies. Therefore, there are needs for novel therapeutic approaches that can address these critical issues. In this direction attempts have been made to improve the bioavailability of various drugs through various carriers such as silica,[18,19] polymers,[20−23] gels,[24,25] lipids,[26,27] oligosaccharides,[28−30] liposomes,[31] various protein cages.[32−40] However, clinically successful carriers are rare and need further development. Apoferritin (Apf) nanocage can encapsulate a large amount of different foreign molecules.[41−46] Apf is a ubiquitous intracellular protein composed of 24 subunits, which self-assemble into a hollow nanocage with an outer diameter of 12 nm and an interior diameter 8 nm.[47] The assembly and disassembly of this protein cage can be regulated by changing pH, as protein cage can be disassociated into all 24 subunits at pH 2.0 and the subunits can be reassembled at neutral pH.[48−50] Thus, the inner core/cavity

is a suitable template for encapsulation of the various drugs such as doxorubicin.[41−45] Recently, it was reported that Apf binds to human cells via interaction with the transferrin receptor 1 (TfR-1),[51] which is overexpressed on human cancer cells.[52,53] In the present study, we have used Apf nanocage without any ligand functionalization for cancer cell specific targeting and delivery of two differentially polar anticancer drugs such as hydrophilic doxorubicin (Dox) and hydrophobic docetaxel (Doc) individually and in combination, which can simultaneously target two intracellular components such as DNA and microtubule, respectively.[9]

■ EXPERIMENTAL SECTION

Reagents. Apoferritin from equine spleen (horse spleen apoferritin) 0.2 μm filtered, doxorubicin, docetaxel, ATP, glycerol, ethylene-bis(oxyethylenenitrilo)tetraacetic acid (EGTA), 4-piperazine-diethanesulfonic acid (PIPES), 4-(dimethylamino)pyridine (DMAP), bovine serum albumin (BSA), guanosine 5′-triphosphate sodium salt hydrate (GTP), 3-(4, 5-dimethylthiazol-2-yl)-2,5-diphenyltetrazolium bromide (MTT), Dulbecco's modified Eagle medium (DMEM), MES, 4′,6-diamidino-2-phenylindole dihydrochloride (DAPI), molecular biology grade trypsin−EDTA solution, dimethylsulfoxide (DMSO), and formaldehyde solution were purchased from Sigma-Aldrich. Potassium chloride and agarose were purchased from Fisher Scientific. TritonX-100 was purchased from SRL. Dimethylsulfoxide and MeOH were purchased from spectrochem. 2-[4-(2-Hydroxyethyl)piperazin-1-yl]ethanesulfonic acid (HEPES) was purchased from Himedia. Penicillin−streptomycin, neutravidin, Alexa Fluor 488 carboxylic acid, succinimidyl ester, and fetal bovine serum (FBS) were purchased from Invitrogen. Rabbit monoclonal anti-α-tubulin (EP1332Y) antibody and goat polyclonal anti-rabbit IgG H&L (Cy3.5) preadsorbed were purchased from Abcam. Annexin V/PI apoptosis detection kit was purchased from Santa Cruz Biotechnology. Bisbenzimide H 33258 (Hoechst) was purchased from Calbiochem. Cover glass bottom dishes were purchased from SPL. Amicon Ultra (centrifugal filter units) was purchased from Millipore Ireland. PD-10 columns were purchased from GE Healthcare UK. All compounds were used without further purification.

Synthesis of Alexa Fluor 568 Labeled Doc. For the synthesis of Alexa Fluor 568 labeled Doc (AF-568Doc), 2 mg (0.0025 mmol) of Doc and 1.5 mg (0.002 mmol) of Alexa Fluor 568 NHS ester (succinimidyl ester) (Molecular Probes) were taken in glass vial and dissolved in 1 mL of DMSO. The mixture was stirred for 48 h in nitrogen atmosphere in the presence of a catalytic amount of DMAP. From ESI-mass spectroscopy m/z = 1639 as 100% mass was obtained, which exactly matches with the mass [M = 1483] of the compound as [M + 4K]+ (Figures S1, S2, and S3 in Supporting Information).

Synthesis of Alexa Fluor 488 Labeled Apf. Apf was labeled using Alexa Fluor 488 (AF-488) protein labeling kit (Molecular Probes). The most reactive lysine residues of Apf were covalently labeled with the labeling kit. The complex was abbreviated as AF-488Apf.

Synthesis of Drug Encapsulated Apf. 100 μL of Apf from equine spleen (horse spleen apoferritin) 0.2 μm filtered (stock concentration 100 μg/mL) was taken in a glass vial. 2 mL of glycine−acetate buffer of pH 2.5 was added to it and stirred in a magnetic stirrer for 10 min. Then for synthesis of Apf-Dox, 350 μL of Dox of stock concentration 1.5 mM or for Apf-Doc synthesis, 21 μL of Doc of stock concentration 10 mM was added into it and stirred for another 15 min. The pH of the solution was then slowly increased to 7.4 by adding 4 M Tris base solution under constant stirring and continuous monitoring of pH through pH meter. Resulting solution was passed through PD-10 column for removal of free drugs. Fractions were collected from PD-10 column. Whole experiment was carried out in 4 °C cold room. Protein containing fractions were identified through Bradford test. Those fractions were concentrated using concentrator of molecular weight cutoff of 100 kDa. Protein complex were collected and stored at −20 °C. Concentration of the drug encapsulated in the

Apf complex was then calculated from standard curve of the respective drug using UV−vis spectrophotometer (Figure S4 in Supporting Information). Dox concentration inside the Apf-Dox complex was found to be 200 μM, whereas Doc concentration inside Apf-Doc complex was found to be 76 μM. We have also calculated the encapsulation efficiency of Apf (Supporting Information), and it was observed to be 80% for Apf-Dox and 76% for Apf-Doc. For dual drug encapsulation above-mentioned amounts of both drugs were added keeping remaining parameters unchanged. For imaging and other fluorometric assays AF-568Doc was encapsulated as above-mentioned concentrations and the complex was abbreviated as Apf-AF-568Doc.

Protein Purification. Tubulin was isolated from goat brain and purified through two cycles of polymerization and depolymerization procedure as in the literature.[54] MES based buffer was used for depolymerization, and high molarity PIPES buffer was used for polymerization along with ATP and GTP. Highly purified tubulin solution, free from microtubule associated proteins and motor proteins, was obtained. The concentration of tubulin solution was determined measuring its absorbance at 280 nm. A 20 mg/mL tubulin stock was prepared in BRB80 buffer and was stored at −80 °C using 10% glycerol as a cryosolvent.

Cell Culture. MCF7 (human breast cancer cell line), HeLa (human cervical cancer cell line), and WI38 (human lungs fibroblast normal cell line) cell lines were purchased from National Centre for Cell Science (NCCS) Pune, India. Cells were cultured at 37 °C in 5% CO₂ humidified atmosphere using Dulbecco's modified Eagle medium (DMEM) supplemented with 10% heat inactivated fetal bovine serum, kanamycin sulfate (110 mg/L), penicillin (50 units/mL), streptomycin (50 μg/mL).

■ RESULTS AND DISCUSSION

First, we performed transmission electron microscopy (TEM) in order to study the morphology of our newly synthesized Apf complexes. TEM images revealed the structure and size of the newly synthesized Apf complexes. From TEM images cubic saucer shaped Apf with an average size of 10.94 nm was found, whereas in the cases of Apf-Dox and Apf-Doc, average sizes of the complexes were 12.34 and 13.24 nm, respectively (Figure 1). The TEM data were further confirmed by dynamic light scattering (DLS) data. From DLS data, the sizes of Apf, Apf-Dox, and Apf-Doc were found to be 10.68, 11.16, and 11.55 nm respectively (Figure S5). Moreover an increase in size was observed in case of Apf complexes when compared to Apf.

Next, we were interested in finding the reason behind the increased size of the Apf complexes. The amount of drug encapsulated in a single Apf molecule may be the cause of the enhancement of the size. For better understanding the drug binding with the horse spleen Apf and the binding affinity with the particular drug, we performed molecular docking study. Blind docking was performed taking either of the drug Dox or Doc as a ligand with native horse spleen ferritin (PDB code 1IES)[55] as a receptor and revealed that the drug binds with horse spleen ferritin with different hydrogen bonding and hydrophobic interactions. We found binding affinity of Dox with horse spleen ferritin was −8.5 kcal/mol (Figure 2a), whereas for Doc binding affinity was found to be −9.5 kcal/mol (Figure 2c). Figure 2b and Figure 2d represent the bonding partners of Dox and Doc with horse spleen ferritin, respectively. This result indicates that Doc has a high binding affinity compared to Dox resulting in binding of a higher number of Doc molecules with horse spleen ferritin, which causes enhancement of size.

Further, Dox molecule being hydrophilic in nature and Doc molecule being hydrophobic in nature and two drugs having two different targets toward cancer cells, we were interested in encapsulating both the drugs simultaneously into the Apf cage.
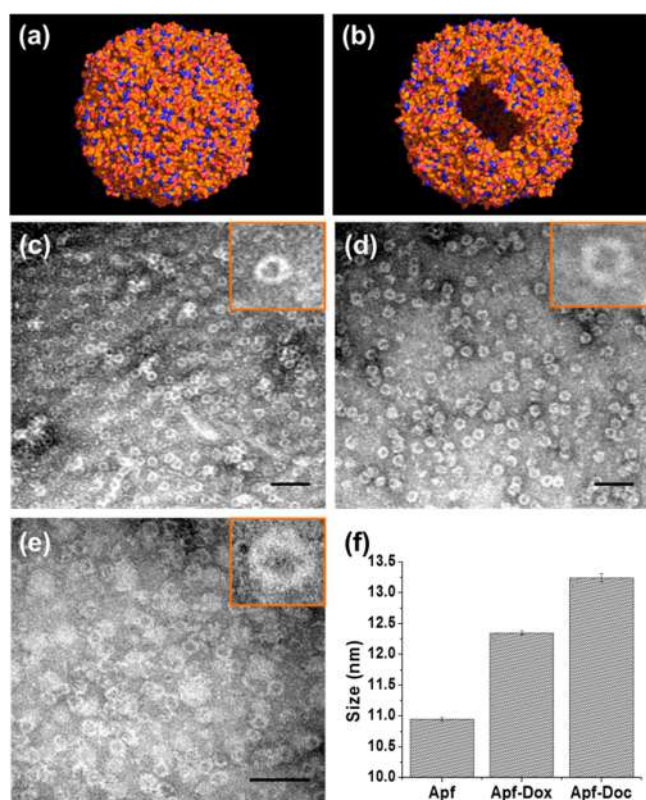
Figure 1. (a) Image shows Apf complex. (b) Image shows hollow core of Apf complex. TEM images: (c) Apf with zoomed image (inset); (d) Apf-Dox with zoomed image (inset); (e) Apf-Doc with zoomed image (inset). (f) Bar diagram representing size variation of different Apf complexes. Scale bars correspond to 50 nm.
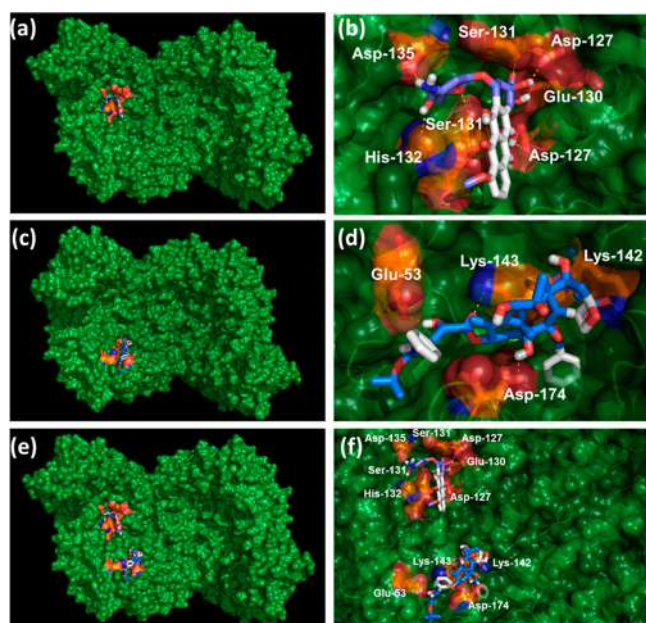

Figure 2. (a) Docking images show binding of Dox to horse spleen ferritin. (b) Bonding partner of Apf when interacting with Dox. (c) Docking images show binding of Doc to horse spleen ferritin. (d) Bonding partner of Apf when interacting with Doc. (e) Docking images show binding of Dox and Doc to horse spleen ferritin. (f) Bonding partner of Apf when interacting with both Dox and Doc.
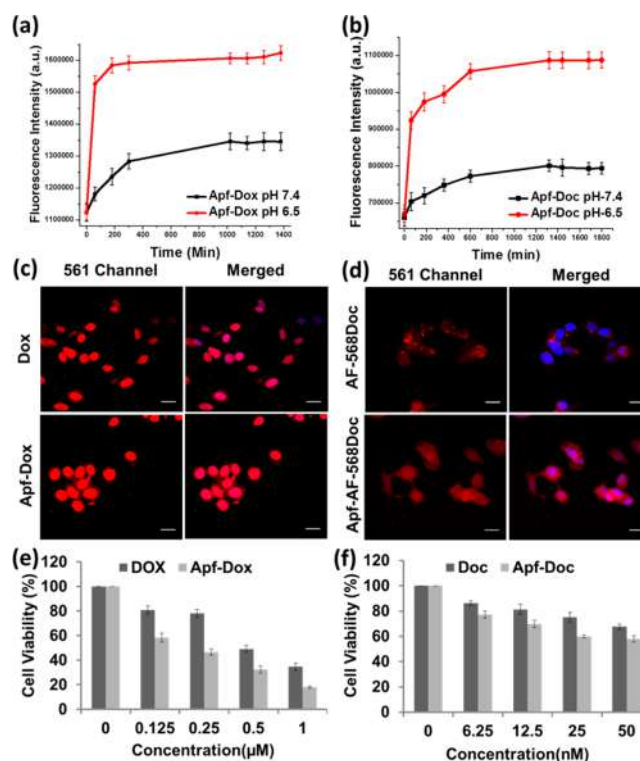

Figure 3. (a) Time dependent in vitro release kinetics of Dox from Apf-Dox complex at different pH. (b) Time dependent in vitro release kinetics of Doc from Apf-Doc complex at different pH. Intracellular drug delivery efficiency of Apf-drug complex: (c) After 4 h of incubation with Apf-Dox and Dox alone, a large intensity of Dox was observed inside nucleus in the case of Apf-Dox compared to Dox alone. (d) Enhanced localization of Doc inside the cancer cell after treatment of cancer cell with Apf-AF-568 Doc compared to AF-568Doc alone. (e) Bar chart shows the comparison of percentage of MCF7 cell viability at different concentrations of Dox and Apf-Dox. (f) Bar chart shows the comparison of percentage of MCF7 cell viability at different concentrations of Doc and Apf-Doc. Scale bars correspond to 20 μm.

Since synergistic effects of both drugs were previously shown[9,10] and individual drug binds with ferritin, we planned to encapsulate dual drugs Dox and Doc simultaneously to horse spleen ferritin. Next, to confirm whether dual drug simultaneously binds horse spleen ferritin or not, we performed dual molecular blind docking with native horse spleen ferritin (PDB code 1IES)[55] as single receptor with two drugs Dox and Doc as two ligands. We found Dox and Doc bind horse spleen ferritin with binding affinities of −8.5 kcal/mol and −9.5 kcal/mol, respectively, at different binding locations (Figure 2e). Figure 2f presents the bonding partners for Dox and Doc.

Additionally, it was reported earlier that tumor microenvironment has higher acidic pH (around 6.5−6.8) compared to normal tissue, as cancer cells strongly depend on glycolysis instead of oxidative phosphorylation for energy consumption to increase biosynthetic functions, leading to an increase rate of lactic acid production.[56,57] On the other hand Apf molecules get dissociated at acidic pH.[58] We tried to exploit both of the properties for selective release of encapsulated drugs in tumor microenvironment. To confirm this, we have performed in vitro time dependent fluorometric release kinetics assay. For this, 10 μM final concentration of Apf-Dox or 50 nM final concentration of Apf-AF-568Doc was prepared in 100 μL of phosphate buffer solution of either pH 6.5 or pH 7.4. For Apf-
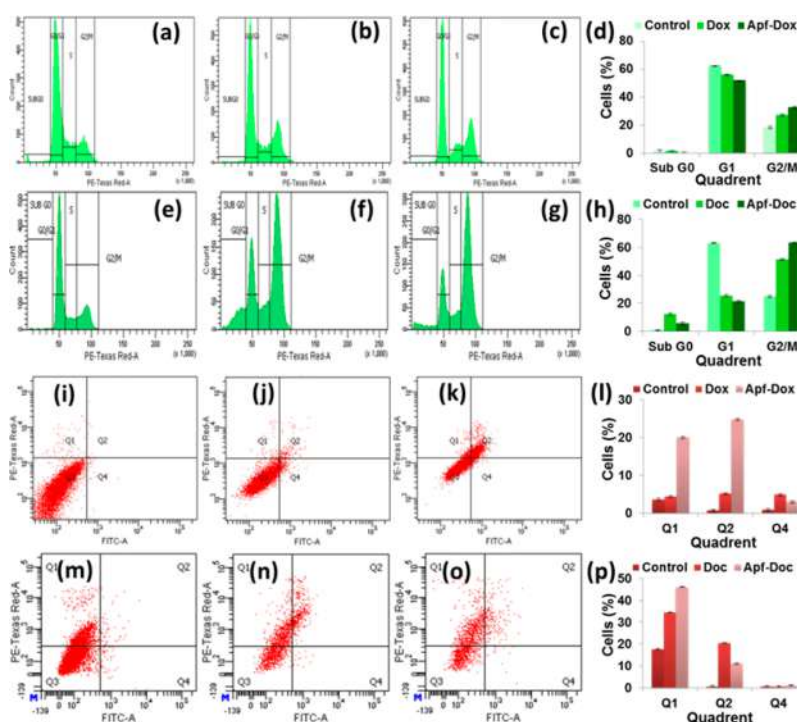
Figure 4. Cell cycle and apoptosis analysis in MCF7 cell line: (a) control or untreated MCF7 cell, (b) treatment with Dox, and (c) treatment with Apf-Dox. (d) Comparative bar diagram representing the % of cells arrested in different phase of cell cycle. Data indicate that Apf-Dox causes higher G2/M arrest. (e) Control or untreated MCF7 cell, (f) treatment with Doc, (g) treatment with Apf-Doc, (h) comparative bar diagram representing the % of cells arrested in different phase of cell cycle. Data indicate that Apf-Doc also causes higher G2/M arrest. FACS analysis showing the amount of apoptotic cell population is increased on Apf-Dox treatment (k), compared to Dox (j) and control (i). (l) Comparative bar diagram representing the % of apoptotic and necrotic cell population. (o) FACS analysis representing increase in amount of necrotic cell population, compared to Doc (n) and control (m). (p) Comparative bar diagram representing the % of apoptotic and necrotic cell population. Quadrants represent the following: Q1, necrotic; Q2, late apoptotic; Q3, healthy; Q4, early apoptotic cells.
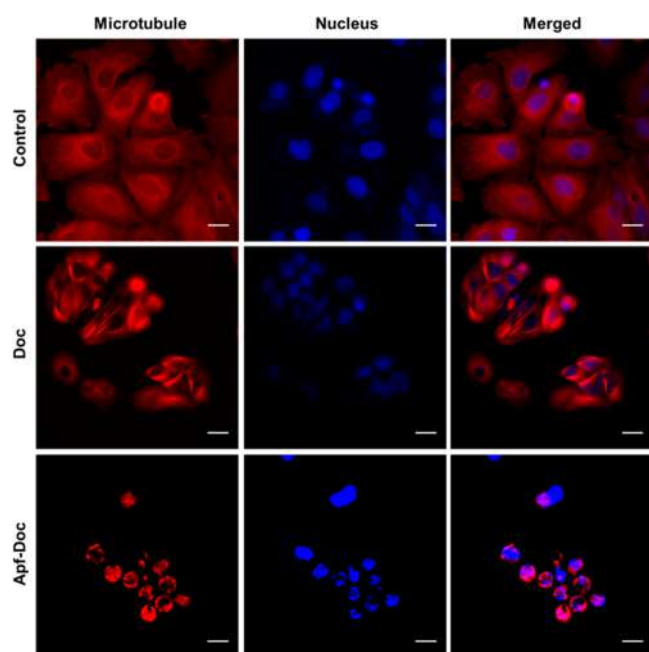

Figure 5. Microtubule network of control, Doc, and Apf-Doc treated MCF7 cells in 561 nm channel indicating nicely distributed microtubule network in control, bundled form of microtubule network on Doc treatment and shrunken and bundled form of microtubule network on Apf-Doc treatment. Images of nucleus were captured at 405 nm channel. Scale bars correspond to 20 μm.
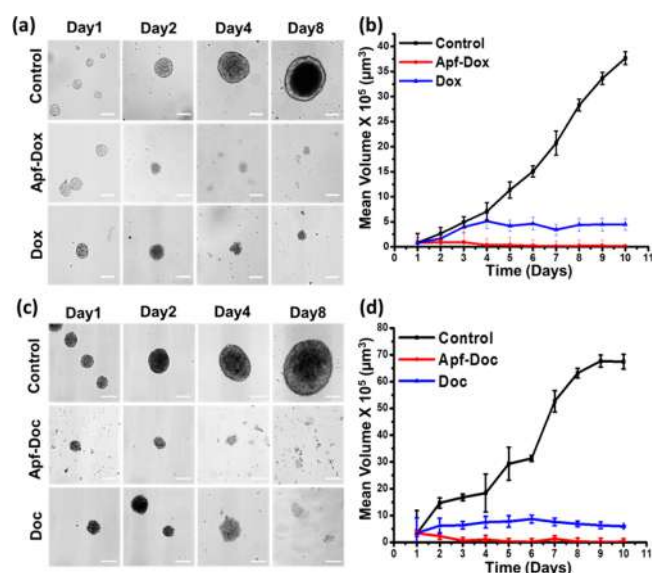

Figure 6. (a) Bright field images represent the size of spheroids from day 1 to day 8 in control, after treatment with Apf-Dox and Dox. (b) Graph shows spheroid growth in control, Apf-Dox, and Dox treated spheroid, which indicates maximum growth inhibition on treatment with Apf-Dox. (c) Bright field images represent the size of spheroids from day 1 to day 8 in control, after treatment with Apf-Doc and Doc. (d) Graph shows spheroid growth in control, Apf-Doc, and Doc treated spheroid, which indicates maximum growth inhibition on treatment with Apf-Doc. Scale bars correspond to 100 μm.
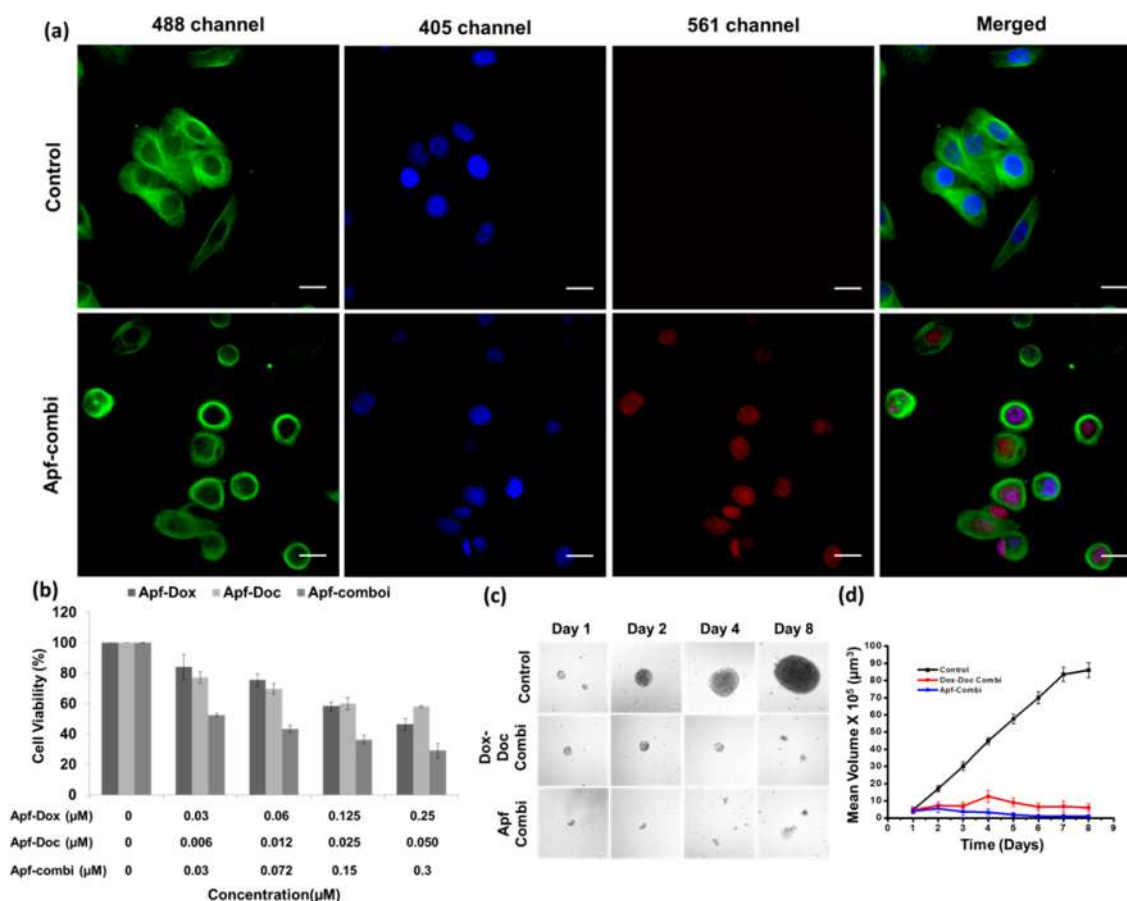
Figure 7. Effect of Apf-Combi on MCF7 cell line. (a) 488 channel representing microtubule network, 405 channel representing nucleus stained by Hoechest, 561 channel representing fluorescence by Dox. In control merged image good microtubule network was observed with blue colored nucleus at its center, whereas on treatment with Apf-Combi, bundled shaped microtubule network with colocalization of Dox at nucleus was observed, indicating encapsulation of both the drugs and their combinatorial effect on MCF7 cells. (b) Comparison of percentage of cells viable at different concentrations of Apf-Dox, Apf-Doc, and Apf-Combi. For Apf-Combi Dox and Doc treatment ratio was 5:1. Scale bars correspond to 20 μm. (c) Bright field images represent the size of spheroids from day 1 to day 8 in control, after treatment with Apf-Combi and Dox-Doc in combination. (d) Graph shows spheroid growth in control, Apf-Combi, and Dox-Doc combination treated spheroid, which indicates maximum growth inhibition on treatment with Apf-Combi. Scale bars correspond to 100 μm.

Dox, excitation and emission maxima were set at 480 and 490−700 nm, respectively, whereas for Apf-AF-568Doc, excitation and emission maxima were at 578 and 590−800 nm, respectively. For both cases an increase in fluorescence intensity with time was observed at pH 6.5 compared to pH 7.4 (Figure 3a and Figure 3b). The result indicates that the complex might be able to release encapsulated drug selectively to tumor microenvironment.

In order to further analyze the intracellular drug delivery efficiency of Apf-Dox complex in comparison with Dox, time dependent intracellular release assay was performed. MCF7 cells were treated with 0.1 μM Apf-Dox and Dox differently. Up to 2 h less localization of Dox around nucleus was observed in the case of Apf-Dox when compared to Dox itself (Figure S6) due to slow release of Dox from Apf-Dox. After 3 h, a slightly higher amount of Dox was released around the nucleus in the case of Apf-Dox compared with Dox treated MCF7 cell. But after 4 h of treatment a significant amount of Dox was localized inside the nucleus in the case of Apf-Dox whereas for Dox treatment concentration of drug inside the nucleus merely changed (Figure 3c and Figure S6). This result suggests that the concentration of Dox is increased in the case of Apf-Dox treated MCF7 cell with time as it slowly releases the drug inside

the cancer cell. Slow release of drug helps in increasing the availability and effectivity of drug inside the cancer cell and protects the drug from degradation. Cellular uptake pathway may have an important role in this regard. Reducing the cellular reflux and pH dependent release may be the reason behind higher localization of the drug around the nucleus.

Furthermore, Doc has a specific target toward microtubule network. Microtubule is one of the cytoskeleton protein that maintains the structure and function of eukaryotic cell. We were interested in checking the cellular uptake of Apf-AF-568Doc inside cancer cells. For that purpose MCF7 cells were treated with 20 nM Apf-AF-568Doc or 20 nM AF-568Doc. After 2 h of incubation a greater uptake of Apf-AF-568Doc was observed throughout the cells in comparison to AF-568Doc (Figure 3d and Figure S7).

The above results motivated us to investigate the mode of internalization of Apf complexes. To understand mode of internalization, we did flow cytometric experiments reported earlier.[59] HeLa cells were treated with AF-488Apf. We observed significant higher uptake of AF-488Apf when incubated at 37 °C compared to the cells incubated at lower temperature (4 °C) (Figure S8). The result supports the involvement of endocytosis as the major mechanism of the internalization. This

study was further supported by recent report that Apf gets internalized into the cancer cells specifically through transferrin receptor 1 (TfR-1),[51] which is overexpressed on human cancer cells.[52,53] On the contrary as Apf gets internalized through endocytosis process, release of the encapsulated drugs specifically takes place inside the endosome of cancer cell, as endosomes has a pH of around 5−6.5.[60,61] We choose MCF7[62] and HeLa[63,64] cells as TfR-1 positive cell line for our further study.

Since we have observed that Apf gets internalized through endocytosis process and it releases encapsulated drug in a pH dependent manner, we became interested in investigating whether Apf-Dox has a better cytotoxicity compared to Dox itself or not. For that, conventional MTT assay was performed. Reduction of 3-(4, 5-dimethylthiazol-2-yl)-2,5-diphenyl-tetrazolium bromide (MTT) to its insoluble formazan is known as MTT assay. MCF7 and HeLa cells were treated with various concentrations of either Apf-Dox or Dox. In the case of MCF7 cells, Apf-Dox showed remarkably higher ∼83% cytotoxicity in comparison to Dox ∼66% (Figure 3e). In the case of HeLa cells cytotoxicity was ∼80% for Apf-Dox where Dox showed ∼64% cytotoxicity (Figure S9a). On the other hand, we were also interested in checking cytotoxicity of Apf-Doc over Doc toward MCF7 cancer cell line following above-described method, which resulted better cytotoxicity of Apf-Doc in comparison to Doc itself (Figure 3f). We were also interested in checking cytotoxicity of Apf-Dox toward WI38 (lung fibroblast cell) normal cell line. We did not observe any significant change in cytotoxicity when compared to Dox itself (Figure S9b). As control experiment we have checked cytotoxicity of the protein complex (Horse spleen Apf) and found no cytotoxicity toward HeLa cancer cells line (Figure S9c). From the above result it was confirmed that potency of drug increases after complexation with Apf and the efficacy enhances toward cancer cell because the drugs were delivered toward cancer cells through receptor mediated pathway, which causes enhanced cytotoxicity.

Next, we performed flow cytometric cell cycle analysis to evaluate the effect of Apf complexes compared to drugs alone in cell cycle. We performed the experiment in MCF7 cells. In the case of Apf-Dox, after treatment with 0.1 μM Apf-Dox and Dox differently, the cells were fixed and PI associated cell cycle analysis was performed in flow cytometer (Supporting Information). The result represents an increased G2/M phase arrest in case of Apf-Dox in comparison to Dox (Figure 4a−d). It has been described before that Dox acts upon DNA topoisomerase II; as a result, fragmented DNA is produced at the time of replication and cells get arrested at G2/M phase.[65] Our result clearly shows that the Apf complex mediated delivery of Dox and increases the potency of Dox. On the contrary, we also checked the impact of Apf-Doc in comparison to Doc alone on cell cycle pathways at a concentration of 20 nM. We found a 63.4% G2/M arrest in the case of Apf-Doc, whereas it was 51.4% for Doc alone (Figure 4e−h). As Doc targets the microtubule network of a cell, it generally arrests the cell cycle at G2/M phase.[66] The result here also proves that efficacy of Doc increases after encapsulation inside Apf.

We were further interested to know the impact of Apf-Dox complex on cellular death pathway in comparison to Dox alone. For that, flow cytometric analysis was performed using annexin-V and propidium iodide (PI). MCF7 cells were treated with 0.1 μM conentration of either Apf-Dox or Dox. The results indicate a sharp increase of late apoptotic ∼24.8% (Q2) and necrotic

∼20.1% (Q1) cell in the case of Apf-Dox whereas for Dox late apoptotic cells were ∼5.2% and necrotic cells were ∼4.4% (Figure 4i−l). This result clearly indicates that Apf-Dox induces higher cell death compared to Dox alone. Similarly, we compared cellular death pathway of Apf-Doc over Doc. MCF7 cells were treated with 20 nM concentration of either Apf-Doc or Doc, and flow cytometric analysis was performed following the method described previously. The result represented here indicates 20.6% late apoptotic (Q2) and 34.5% necrotic cells (Q1) in the case of Doc treatment, whereas a sharp increase in necrotic cells 46.1% (Q1) was observed upon treatment with Apf-Doc (Figure 4m−p). This is due to mitotic catastrophe, as it was described earlier that mitotic catastrophe is a mode of cell death that results from premature or inappropriate entry of the cells into mitosis.[67] Doc is one of the drugs that induce mitotic catastrophe.[67] Thus, the above result clearly indicates that receptor mediated selective delivery through Apf induces the efficacy of both drugs compared to bare drugs.

The above results motivated us to investigate whether Apf-Doc has better effect over Doc toward intracellular microtubule network or not, as Doc has a specific target binding site to tubulin. MCF7 cells were treated for 24 h with 20 nM Apf-Doc and Doc differently. The cells were then immunostained with anti-α-tubulin primary antibody and Cy3.5 labeled anti IgG secondary antibody (Supporting Information). The cell images were captured under fluorescence microscope (Olympus IX83) with a 40× objective (Figure 5). Interestingly, the result shows that Apf-Doc disrupts intracellular microtubule network and changes the cellular morphology in comparison to Doc alone whereas the image of control cell (untreated) provides a nice microtubules network. This result also demonstrated the enhanced efficacy of Doc after complexation with Apf.

Further, we have checked the binding affinity of Apf toward tubulin/microtubule. Tubulin is monomeric unit of micro-tubule composed of α and β subunits. The binding affinity of Apf with tubulin was determined by measuring the rate of tryptophan (Trp) fluorescence quenching of tubulin after interaction with different concentrations of Apf (Supporting Information). Intrinsic Trp fluorescence of tubulin is quenched upon binding of Apf with tubulin and indicates that its binding with tubulin perturbs tubulin conformation in the vicinity of Trp residues. The binding constant was calculated as 18.2×10^3 M^{-1} (Figure S10) using a modified Stern−Volmer equation,[68] which indicates significant binding of Apf with tubulin.

Next, we studied the efficacy of Apf complexes in 3D multicellular tumor spheroid model because efficacy of therapeutic molecules validated in 2D cell culture often fails to show potential in in vivo system. It is important to note that 3D multicellular tumor model successfully mimics in vivo tumor as it has growth kinetics, morphology, and micro-environment similar to in vivo tumor. Here, 3D spheroid was prepared from HeLa monolayer cells using liquid overlay method.[69] HeLa cells are TfR-1 positive cell line, which will facilitate internalization of Apf-complex. Growth delay experi-ment was performed following the previously described method.[70] Four sets of well grown tumor spheroids (after 4 days from the generation of spheroid) were separately treated with Apf-Dox (1 μM), Dox (1 μM), Apf-Doc (50 nM), and Doc (50 nM) along with untreated control for each group for comparison of growth inhibition. Both treated and control spheroids were imaged under inverted microscope using Z-stack, and the volume of the spheroid was measured up to 8

days from the day of treatment. We found a significant growth inhibition in the case of both Apf-drug complexes in comparison to drugs alone, whereas a significant increase in spheroid volume was found in the case of control group (Figure 6). This result supports the tumor specific receptor mediated uptake and pH dependent release of drugs from Apf-complex. This result also confirms that Apf is an excellent system for delivering both hydrophobic and hydrophilic drugs in a targeted manner.

Since Apf can successfully deliver both hydrophobic (Doc) and hydrophilic (Dox) drugs, we became interested to study whether Apf can deliver both drugs as combination. Thus, we prepared Apf encapsulated Dox and Doc drugs complex (Apf-Combi). MCF7 cells were treated with Apf-Combi with a Dox final concentration of 0.1 μM and Doc final concentration of 20 nM along with untreated or control set of experiment. It has been described before that Dox acts as topoisomerase II inhibitor and binds with DNA and Doc acts as microtubule stabilizing drug and forms bundle-like structure of intracellular microtubule network. Microtubule was stained with anti-α-tubulin primary antibody (clone EP 1332Y rabbit monoclonal antibody) (1:300) for 2 h followed by treatment with FITC tagged IgG secondary antibody (Merck Millipore) (1:500) for further 2 h. Fluorescence microscopic images reveal significant effect on microtubule network, as bundle-like microtubules were formed and significant uptake of Dox in the nucleus was observed. This result clearly represents that Apf can successfully deliver both drugs simultaneously (Figure 7a). Further, we have studied the cytotoxicity of Apf-Combi using MTT assay following the above-mentioned method. MCF7 cells were treated with different concentrations of Apf-Dox, Apf-Doc, and Apf-Combi along with untreated control. MTT result reveals significant enhancement of cell cytotoxicity when treated with Apf-Combi compared to individually treated Apf-Dox and Apf-Doc complexes (Figure 7b). The above result clearly demonstrated that Apf protein complex served as an excellent platform for delivering combination of both hydrophobic and hydrophilic drugs simultaneously in a targeted fashion and exerted significant cytotoxic effect.

Finally, we studied the effect of Apf-Combi on 3D multicellular tumor spheroid model. We prepared HeLa cell spheroid following the aforesaid method. Three sets of well grown tumor spheroids (after 4 days from the generation of spheroid) were separately treated with either Apf-Combi with a Dox final concentration of ~1 μM and Doc final concentration of ~0.2 μM or combination of Dox (1 μM) and Doc (0.2 μM) along with an untreated control for comparison of growth inhibition. Both treated and control spheroids were imaged under inverted microscope using Z-stack, and the volume of the spheroid was measured up to 8 days from the day of treatment. We found a significant growth inhibition in the case of Apf-Combi in comparison to drugs combination, whereas a significant increase in spheroid volume was observed in the case of control group (Figure 7c and Figure 7d). The result itself clearly shows that Apf possesses a substantial activity of targeting cancer cells and acts as an excellent system for delivering combination of drugs in targeted manner.

CONCLUSION

In summary, this manuscript clearly demonstrates that Apf serves as an excellent platform for delivering both Dox and Doc drugs individually into the cancer cell in a targeted fashion. In addition, Apf also delivers both drugs simultaneously into the cancer cell in a targeted manner and exerts combination anticancer effect. We envision that the Apf-based combination drug delivery vehicle will be an excellent anticancer therapeutic formulation in the near future.

ASSOCIATED CONTENT

ⓢ Supporting Information

The Supporting Information is available free of charge on the ACS Publications website at DOI: 10.1021/acsami.6b11798.

Quantification of concentration of encapsulated drug in Apf and calculation of loading efficiency, transmission electron microscopy (TEM), dynamic light scattering (DLS), docking, cellular uptake study, determination of cellular internalization pathway through flow cytometry, evaluation of cell viability, cell cycle analysis by flow cytometry, apoptosis study by flow cytometry, effect of Apf-Doc in comparison to Doc on intracellular micro-tubule network of MCF7 cells, determination of binding affinity of Apo with tubulin by fluorescence intensity quenching of intrinsic tryptophan residue of tubulin, generation of multicellular tumor spheroidal (3D spheroid) cultures and treatment (PDF)

AUTHOR INFORMATION

Corresponding Author

*E-mail: sghosh@iicb.res.in. Fax: +91-33-2473-5197/0284. Phone: +91-33-2499-5872.

Notes

The authors declare no competing financial interest.

ACKNOWLEDGMENTS

REFERENCES

(1) Minchinton, A. I.; Tannock, I. F. Drug Penetration in Solid Tumours. Nat. Rev. Cancer 2006, 6, 583−592.

(2) Cieslewicz, M.; Tang, J.; Yu, J. L.; Cao, H.; Zavaljevski, M.; Motoyama, K.; Lieber, A.; Raines, E. W.; Pun, S. H. Targeted Delivery of Proapoptotic Peptides to Tumor-associated Macrophages Improves survival. Proc. Natl. Acad. Sci. U. S. A. 2013, 110, 15919−24.

(3) Gottesman, M. M. Mechanisms of Cancer Drug Resistance. Annu. Rev. Med. 2002, 53, 615−627.

(4) Keith, C. T.; Borisy, A. A.; Stockwell, B. R. Multicomponent Therapeutics for Networked Systems. Nat. Rev. Drug Discovery 2005, 4, 71−78.

(5) Honore, S.; Kamath, K.; Braguer, D.; Horwitz, S. B.; Wilson, L.; Briand, C.; Jordan, M. A. Synergistic Suppression of Microtubule Dynamics by Discodermolide and Paclitaxel in Non-Small Cell Lung Carcinoma Cells. Cancer Res. 2004, 64, 4957−4964.

(6) Lee, M. S.; Johansen, L.; Zhang, Y.; Wilson, A.; Keegan, M.; Avery, W.; Elliott, P.; Borisy, A. A.; Keith, C. T. The Novel Combination of Chlorpromazine and Pentamidine Exerts Synergistic Antiproliferative Effects Through Dual Mitotic Action. Cancer Res. 2007, 67, 11359−11367.

(7) Milane, L.; Duan, Z.; Amiji, M. Development of EGFR-targeted Polymer Blend Nanocarriers for Combination Paclitaxel/lonidamine Delivery to Treat Multi-drug Resistance in Human Breast and Ovarian Tumor Cells. Mol. Pharmaceutics 2011, 8, 185−203.

(8) Schwartz, J. Current Combination Chemotherapy Regimens for Metastatic Breast Cancer. *Am. J. Health-Syst. Pharm.* **2009**, *66*, 3−8.

(9) Tsakalozou, E.; Eckman, A. M.; Bae, Y. Combination Effects of Docetaxel and Doxorubicin in Hormone-Refractory Prostate Cancer Cells. *Biochem. Res. Int.* **2012**, *2012*, 1−10.

(10) Nabholtz, J. M. Docetaxel (Taxotere) Plus Doxorubicin-based Combinations: The Evidence of Activity in Breast Cancer. *Semin. Oncol.* **1999**, *26*, 7−13.

(11) Itoh, K.; Sasaki, Y.; Fujii, H.; Minami, H.; Ohtsu, T.; Wakita, H.; Igarashi, T.; Watanabe, Y.; Onozawa, Y.; Kashimura, M.; Ohashi, Y. Study of Dose Escalation and Sequence Switching of Administration of the Combination of Docetaxel and Doxorubicin in Advanced Breast Cancer. *Clin. Cancer Res.* **2000**, *10*, 4082−4090.

(12) Ricevuto, E.; Cocciolone, V.; Mancini, M.; Cannita, K.; Romano, S.; Bruera, G.; Pelliccione, M.; Adinolfi, M. I.; Ciccozzi, A.; Bafile, A.; Penco, M.; Ficorella, C. Dose-Dense Nonpegylated Liposomal Doxorubicin and Docetaxel Combination in Breast Cancer: Dose-Finding Study. *Oncologist* **2015**, *20*, 109−110.

(13) Kim, Y. H.; Shin, S. W.; Kim, B. S.; Kim, J. H.; Kim, J. G.; Mok, Y. J.; Kim, C. S.; Rhyu, H. S.; Hyun, J. H.; Kim, J. S. Paclitaxel, 5-Fluorouracil, and Cisplatin Combination Chemotherapy for the Treatment of Advanced Gastric Carcinoma. *Cancer* **1999**, *85*, 295−301.

(14) Paul, D. M.; Garrett, A. M.; Meshad, M.; DeVore, R. D.; Porter, L. L.; Johnson, D. H. Paclitaxel and 5-Fluorouracil in Metastatic Breast Cancer: the US Experience. *Semin. Oncol.* **1996**, *23*, 48−52.

(15) Smorenburg, C. H.; Sparreboom, A.; Bontenbal, M.; Verweij, J. Combination Chemotherapy of the Taxanes and Antimetabolites: Its Use and Limitations. *Eur. J. Cancer* **2001**, *37*, 2310−2323.

(16) Schmiegelow, K.; Nielsen, S. N.; Frandsen, T. L.; Nersting, J. Mercaptopurine/Methotrexate Maintenance Therapy of Childhood Acute Lymphoblastic Leukemia: Clinical Facts and Fiction. *J. Pediatr. Hematol./Oncol.* **2014**, *36*, 503−517.

(17) Chabner, B. A.; Roberts, T. G., Jr. Timeline: Chemotherapy and the War on Cancer. *Nat. Rev. Cancer* **2005**, *5*, 65−72.

(18) Barbé, C.; Bartlett, J.; Kong, L.; Finnie, K.; Lin, H. Q.; Larkin, M.; Calleja, S.; Bush, A.; Calleja, G. Silica Particles: A Novel Drug-Delivery System. *Adv. Mater.* **2004**, *16*, 1959−1966.

(19) Argyo, C.; Weiss, V.; Bräuchle, C.; Bein, T. Multifunctional Mesoporous Silica Nanoparticles as a Universal Platform for Drug Delivery. *Chem. Mater.* **2014**, *26*, 435−451.

(20) Kumari, A.; Yadav, S. K.; Yadav, S. C. Biodegradable Polymeric Nanoparticles Based Drug Delivery Systems. *Colloids Surf., B* **2010**, *75*, 1−18.

(21) Liechty, W. B.; Kryscio, D. R.; Slaughter, B. V.; Peppas, N. A. Polymers for Drug Delivery Systems. *Annu. Rev. Chem. Biomol. Eng.* **2010**, *1*, 149−73.

(22) Schmaljohann, D. Thermo- and pH-responsive Polymers in Drug Delivery. *Adv. Drug Delivery Rev.* **2006**, *58*, 1655−1670.

(23) Allen, T. M.; Cullis, P. R. Drug Delivery Systems: Entering the Mainstream. *Science* **2004**, *303*, 1818−1822.

(24) Qiu, Y.; Park, K. Environment-sensitive Hydrogels for Drug Delivery. *Adv. Drug Delivery Rev.* **2012**, *64*, 49−60.

(25) Shah, J. C.; Sadhale, Y.; Chilukuri, D. M. Cubic Phase Gels as Drug Delivery Systems. *Adv. Drug Delivery Rev.* **2001**, *47*, 229−250.

(26) Porter, C. J. H.; Trevaskis, N. L.; Charman, W. N. Lipids and Lipid-based Formulations: Optimizing the Oral Delivery of Lipophilic Drugs. *Nat. Rev. Drug Discovery* **2007**, *6*, 231−248.

(27) Shrestha, H.; Bala, R.; Arora, S. Lipid-Based Drug Delivery Systems. *J. Pharm.* **2014**, *2014*, 1−10.

(28) Seeberger, P. H.; Werz, D. B. Automated Synthesis of Oligosaccharides as a Basis for Drug Discovery. *Nat. Rev. Drug Discovery* **2005**, *4*, 751−763.

(29) Pouyani, T.; Prestwich, G. D. Functionalized Derivatives of Hyaluronic Acid Oligosaccharides: Drug Carriers and Novel Biomaterials. *Bioconjugate Chem.* **1994**, *5*, 339−347.

(30) Termsarasab, U.; Cho, H. J.; Kim, D. H.; Chong, S.; Chung, S. J.; Shim, C. K.; Moon, H. T.; Kim, D. D. Chitosan Oligosaccharide−

arachidic Acid-based Nanoparticles for Anti-cancer Drug Delivery. *Int. J. Pharm.* **2013**, *441*, 373−380.

(31) Bangham, A. D.; Standish, M. M.; Watkins, J. C. Diffusion of Univalent Ions Across the Lamellae of Swollen Phospholipids. *J. Mol. Biol.* **1965**, *13*, 238−252.

(32) Maham, A.; Tang, Z.; Wu, H.; Wang, J.; Lin, Y. H. Protein-Based Nanomedicine Platforms for Drug Delivery. *Small* **2009**, *5*, 1706−1721.

(33) Molino, N. M.; Wang, S. W. Caged Protein Nanoparticles for Drug Delivery. *Curr. Opin. Biotechnol.* **2014**, *28*, 75−82.

(34) Wu, H.; Engelhard, M. H.; Wang, J.; Fisher, D. R.; Lin, Y. H. Synthesis of Lutetium phosphate−apoferritin Core−shell Nanoparticles for Potential Applications in Radioimmunoimaging and Radioimmunotherapy of Cancers. *J. Mater. Chem.* **2008**, *18*, 1779−1783.

(35) Uchida, M.; Flenniken, M. L.; Allen, M.; Willits, D. A.; Crowley, B. E.; Brumfield, S.; Willis, A. F.; Jackiw, L.; Jutila, M.; Young, M. J.; Douglas, T. Targeting of Cancer Cells with Ferrimagnetic Ferritin Cage Nanoparticles. *J. Am. Chem. Soc.* **2006**, *128*, 16626−16633.

(36) Zhen, Z.; Tang, W.; Chen, H.; Lin, X.; Todd, T.; Wang, G.; Cowger, T.; Chen, X.; Xie, J. RGD-Modified Apoferritin Nanoparticles for Efficient Drug Delivery to Tumors. *ACS Nano* **2013**, *7*, 4830−4837.

(37) Douglas, T.; Young, M. Viruses: Making Friends with Old Foes. *Science* **2006**, *312*, 873−875. (h) Ma, Y.; Nolte, R. J. M.; Cornelissen, J. Virus-based Nanocarriers for Drug Delivery. *Adv. Drug Delivery Rev.* **2012**, *64*, 811−825.

(38) Douglas, T.; Young, M. Host−guest Encapsulation of Materials by Assembled Virus Protein Cages. *Nature* **1998**, *393*, 152−155.

(39) Lewis, J. D.; Destito, G.; Zijlstra, A.; Gonzalez, M. J.; Quigley, J. P.; Manchester, M.; Stuhlmann, H. Viral Nanoparticles as a Tools for Intravital Vascular Imaging. *Nat. Med.* **2006**, *12*, 354−360.

(40) Aljabali, A. A.; Shukla, S.; Lomonossoff, G. P.; Steinmetz, N. F.; Evans, D. J. CPMV-DOX Delivers. *Mol. Pharmaceutics* **2013**, *10*, 3−10.

(41) Luo, Y.; Wang, X.; Du, D.; Lin, Y. Hyaluronic Acid-conjugated Apoferritin Nanocages for Lung Cancer Targeted Drug Delivery. *Biomater. Sci.* **2015**, *3*, 1386−1394.

(42) Heger, Z.; Skalickova, S.; Zitka, O.; Adam, V.; Kizek, R. Apoferritin Applications in Nanomedicine. *Nanomedicine (London, U. K.)* **2014**, *9*, 2233−2245.

(43) Hainfeld, J. F. Uranium-loaded Apoferritin with Antibodies Attached: Molecular Design for Uranium Neutron-capture Therapy. *Proc. Natl. Acad. Sci. U. S. A.* **1992**, *89*, 11064−11068.

(44) Cutrin, J. C.; Crich, S. G.; Burghelea, D.; Dastrù, W.; Aime, S. Curcumin/Gd Loaded Apoferritin: A Novel "theranostic" Agent to Prevent Hepatocellular Damage in Toxic Induced Acute Hepatitis. *Mol. Pharmaceutics* **2013**, *10*, 2079−2085.

(45) Xing, R.; Wang, X.; Zhang, C.; Zhang, Y.; Wang, Q.; Yang, Z.; Guo, Z. Characterization and Cellular Uptake of Platinum Anticancer Drugs Encapsulated in Apoferritin. *J. Inorg. Biochem.* **2009**, *103*, 1039−1044.

(46) Fan, R.; Chew, S. W.; Cheong, V. V.; Orner, B. P. Fabrication of Gold Nanoparticles Inside Unmodified Horse Spleen Apoferritin. *Small* **2010**, *6*, 1483−1487.

(47) Theil, E. C. Ferritin: Structure, Gene regulation, and Cellular Function in Animals, Plants, and Microorganisms. *Annu. Rev. Biochem.* **1987**, *56*, 289−315.

(48) Harrison, P. M.; Gregory, D. W. Reassembly of Apoferritin Molecules from Subunits. *Nature* **1968**, *220*, 578−580.

(49) Ma-Ham, A.; Wu, H.; Wang, J.; Kang, X.; Zhang, Y.; Lin, Y. Apoferritin-based Nanomedicine Platform for Drug Delivery: Equilibrium Binding Study of Daunomycin with DNA. *J. Mater. Chem.* **2011**, *21*, 8700−8708.

(50) Ponta, H.; Sherman, L.; Herrlich, P. A. CD44: From Adhesion Molecules To Signalling Regulators. *Nat. Rev. Mol. Cell Biol.* **2003**, *4*, 33−45.

(51) Li, L.; Fang, C. J.; Ryan, J. C.; Niemi, E. C.; Lebrón, J. A.; Björkman, P. J.; Torti, F. M.; Torti, S. V.; Nakamura, M. C.; Seaman, W. E. Binding and Uptake of H-ferritin are Mediated by Human

Transferring Receptor-1. *Proc. Natl. Acad. Sci. U. S. A.* **2010**, *107*, 3505−3510.

(52) Fan, K.; Cao, C.; Pan, Y.; Lu, D.; Yang, D.; Feng, J.; Song, L.; Liang, M.; Yan, X. Magnetoferritin Nanoparticles for Targeting and Visualizing Tumour Tissues. *Nat. Nanotechnol.* **2012**, *7*, 459−464.

(53) Ryschich, E.; Huszty, G.; Knaebel, H. P.; Hartel, M.; Büchler, M. W.; Schmidt, J. Transferrin Receptor is a Marker of Malignant Phenotype in Human Pancreatic Cancer and in Neuroendocrine Carcinoma of the Pancreas. *Eur. J. Cancer* **2004**, *40*, 1418−1422.

(54) Castoldi, M.; Popov, A. V. Purification of Brain Tubulin through Two Cycles of Polymerization−Depolymerization in a High-Molarity Buffer. *Protein Expression Purif.* **2003**, *32*, 83−88.

(55) Granier, T.; Gallois, B.; Dautant, A.; D'Estaintot, B. L.; Precigoux, G. Comparison of the Structures of the Cubic and Tetragonal Forms of Horse-Spleen Apoferritin. *Acta Crystallogr., Sect. D: Biol. Crystallogr.* **1997**, *53*, 580−587.

(56) Du, J.; Lane, L. A.; Nie, S. Stimuli-responsive Nanoparticles for Targeting the Tumor Microenvironment. *J. Controlled Release* **2015**, *219*, 205−214.

(57) Webb, B. A.; Chimenti, M.; Jacobson, M. P.; Barber, D. L. Dysregulated pH: a perfect storm for cancer progression. *Nat. Rev. Cancer* **2011**, *11*, 671−677.

(58) Kim, M.; Rho, Y.; Jin, K. S.; Ahn, B.; Jung, S.; Kim, H.; Ree, M. pH-Dependent Structures of Ferritin and Apoferritin in Solution: Disassembly and Reassembly. *Biomacromolecules* **2011**, *12*, 1629−1640.

(59) Richard, J. P.; Melikov, K.; Vives, E.; Ramos, C.; Verbeure, B.; Gait, M. J.; Chernomordik, L. V.; Lebleu, B. Cell-Penetrating Peptides. A Reevaluation of The Mechanism Of Cellular Uptake. *J. Biol. Chem.* **2003**, *278*, 585−590.

(60) Mindell, J. A. Lysosomal Acidification Mechanisms. *Annu. Rev. Physiol.* **2012**, *74*, 69−86.

(61) Scott, C. C.; Gruenberg, J. Ion Flux and the Function of Endosomes and Lysosomes: pH is Just the Start. *BioEssays* **2011**, *33*, 103−110.

(62) Du, W.; Fan, Y.; He, B.; Zheng, N.; Yuan, L.; Dai, W.; Zhang, H.; Wang, X.; Wang, J.; Zhang, X.; Zhang, Q. Bionano Interactions of MCF-7 Breast Tumor Cells with a Transferrin Receptor Targeted Nanoparticle. *Mol. Pharmaceutics* **2015**, *12*, 1467−1476.

(63) Ward, J. H.; Jordan, I.; Kushner, J. P.; Kaplan, J. Heme Regulation of HeLa Cell Transferrin Receptor Number. *J. Biol. Chem.* **1984**, *259*, 13235−13240.

(64) Roy, C. N.; Penny, D. M.; Feder, J. N.; Enns, C. A. The Hereditary Hemochromatosis Protein, HFE, Specifically Regulates Transferrin-mediated Iron Uptake in HeLa Cells. *J. Biol. Chem.* **1999**, *274*, 9022−9028.

(65) Pommier, Y.; Leo, E.; Zhang, H.; Marchand, C. DNA Topoisomerases and Their Poisoning by Anticancer and Antibacterial Drugs. *Chem. Biol.* **2010**, *17*, 421−433.

(66) Hernández-Vargas, H.; Palacios, J.; Moreno-Bueno, G. Molecular Profiling of Docetaxel Cytotoxicity in Breast Cancer Cells: Uncoupling of Aberrant Mitosis and Apoptosis. *Oncogene* **2007**, *26*, 2902−2913.

(67) Morse, D. L.; Gray, H.; Payne, C. M.; Gillies, R. J. Docetaxel Induces Cell Death through Mitotic Catastrophe in Human Breast Cancer Cells. *Mol. Cancer Ther.* **2005**, *4*, 1495−1504.

(68) Chakraborti, S.; Das, L.; Kapoor, A. N.; Dwivedi, V.; Poddar, A.; Chakraborti, G.; Janik, M.; Basu, G.; Panda, D.; Chakrabarti, P.; Surolia, A.; Bhattacharyya, B. Curcumin Recognizes a Unique Binding Site of Tubulin. *J. Med. Chem.* **2011**, *54*, 6183−6196.

(69) Friedrich, J.; Seidel, C.; Ebner, R.; Kunz-Schughart, L. A. Spheroid-based Drug Screen: Considerations and Practical Approach. *Nat. Protoc.* **2009**, *4*, 309−324.

(70) Wang, L.; Guo, H.; Lin, C.; Yang, L.; Wang, X. Enrichment and Characterization of Cancer Stem-like Cells from a Cervical Cancer Cell Line. *Mol. Med. Rep.* **2014**, *9*, 2117−2123.